POLITECNICO DI TORINO

Master's Degree in Nanotechnologies for ICTs, Micro and Nano Integrated Systems



Master's Degree Thesis

In situ photoemission study of HgTe
 Quantum Dots for photodetectors:
 Functionalization via Alkali Deposition
 and Effects of Low Temperature

Supervisors

Prof. FRANCESCO BERTAZZI

Dr. DEBORA PIERUCCI

Dr. EMMANUEL LHUILLIER

Candidate

GIORGIA STROBBIA

SEPTEMBER 2025

Summary

This research investigates the electronic properties of Mercury Telluride (HgTe) Quantum Dots (QDs), a material of growing interest for infrared optoelectronic applications, particularly as an active layer in photodetectors. The primary characterization technique used is X-ray Photoemission Spectroscopy (XPS), which allows to probe the occupied electronic states of the surface.

A first key focus is the effect of cesium (Cs) deposition on the QD surface. Building on prior studies showing that alkali metals can lower the work function of semiconductors and metals, we demonstrate a strong increase in the Cs 3d core level signal after successive depositions, confirming the effectiveness of the progressive deposition process.

The second aspect of the study explores the influence of operating temperature, with XPS measurements performed between 25°C and 100°C. The results reveal significant shifts in both the valence band and core level energies, which directly affect majority carrier populations and, consequently, the electrical behavior of transistors incorporating HgTe QDs.

Disclaimer

I hereby declare that I have independently written this thesis and that all sources and tools used have been appropriately acknowledged. In the preparation of this document, I made use of Large Language Models (LLM), solely for the purpose of improving the clarity, grammar, and fluency of the text. The use of these tool was limited to language editing and did not influence the intellectual content, analysis, or scientific contributions of the thesis.

Acknowledgements

First of all, I want to express my deepest gratitude to my supervisor Debora Pierucci and to Emmanuel Lhuillier. Thank to you, this work has been an invaluable learning experience, allowing me to explore a wide variety of fields, from cleanroom fabrication to chemistry based work and to a big part of the photoemission field. It was also a great insight on all things that go into research, from the day to day data reporting to organising conferences and workshop.

Another big thank goes to all the members of the OCN team. Each of you taught me a lot, while still maintaining the environment welcoming and making me feel a real member of the team. Special thank for this work go to Dario, an invaluable guide for all my experiments, Mariarosa, for her knowledge and practical approach on all things photoemission and device related. Another big shoutout goes to Adrian, Albin, Alexandre, Clement, Huichen, Matias, Tommaso, always lending an hand and dispensing tricks on how to make things works. Another big thank go to my fellow interns, fantastic companions: Marco, Dries, Jiho, Yanjun, Severin and Francesco.

I also want to thank all the professors and personnel that make Nanotech MNIS possible. Studying at three different prestigious universities, in three different countries, gaining theoretical knowledge and first-hand lab experience, was an honor and one of the most fantastic experience of my life.

Thank to my Nano20 class, who were fantastic colleagues, allies and friends during this beautiful and challenging two years. You were instrumental in my learning and growth, and sometimes in my survival. Acknowledging what each of you has done would require tens of pages, but meeting you hasmaybe been the biggest gift of this program.

An additional big thanks goes to all the people we met along the way and became part of this journey.

I also want to thank my Forchetta friends, who were fundamental for my Bachelor's studies and continued to be there for my Master's.

To my friends from home, I want to thank you all for unwavering support. My deepest gratitude goes to Martina, Arianna, Sara S. and Sara B., who has seen it all as my Turin roommate.

Finally, I want to thank my family and especially my brother, which would never admit it, but is my biggest fan, my grandparents, that sparked my love for learning, and my parents, who made every one of my achievement possible with their love and support.

Table of Contents

	Dis	sclaimer		2
Li	st of	f Tables		7
Li	st of	f Figures		8
A	crony	yms		11
1	Intr	roduction	:	13
	1.1	The laboratory and the OCN gr	oup	13
	1.2	Colloidal Quantum Dots		14
		1.2.1 Quantum confinement .		14
		1.2.2 Colloidal quantum dots		16
	1.3		· ·	19
		9		19
		, , , , , , , , , , , , , , , , , , ,	,	21
			~ ·	22
		· -	·	23
		9 1		24
	1.4			27
			1 1	27
				29
				30
			· ·	33
		v -	ectroscopy (XPS) and Hard X-ray photoemission	ດ 4
		,		34
		1.4.6 In situ and Operando co	ncepts	36
2	Exp	periments, Materials and Me	hods	37
	2.1	Samples' preparation		37
	2.2	Photoemission set-up		38
	2.3	Photoemission measurements .		40
	2.4	Data processing: peak fitting .		42
3	Alk	cali deposition for reduction o	of the work function	45
	3.1	-	ers, doping, and other electronic structure variation	45
				47
	3.2			48

4	Pho	otoemission study of HgTe at low temperature	59
	4.1	General contest	59
		4.1.1 Photodetectors: Dark current and lowering temperature	59
		4.1.2 Band gap trend in temperature in HgTe Quantum Dots	60
	4.2	Measurements and data processing	61
		4.2.1 Samples' characterization and intermediate data processing	62
	4.3	Results and discussion	69
		4.3.1 Peaks and VB	69
		4.3.2 Work function	74
5		nclusions	76
	5.1	Conclusions	76
A	Bac	ekground in XPS data: mathematical definition	78
В	Sup	oplementary information's on XPS acquisition	79
Βi	blios	graphy	81

List of Tables

1.1	Spin-orbit splitting: j values and area ratios for different subshells	31
2.1	Fit of Hg4f	43
2.2	Fit of Te 4d	44
3.1	Fitting parameter for Cs 3d	51
3.2	Fit of Hg4f on pristine sample	
3.3	Fit of Hg4f after 3 minutes of Cs deposition	53
3.4	Fit of Hg4f after 6 minutes of Cs deposition	53
3.5	Fit of Te 4d on pristine sample	53
3.6	Fit of Te 4d after 3 minutes of Cs deposition	54
	Fit of Te 4d after 6 minutes of Cs deposition	
B.1	Peaks taken on the XPS set-up	79

List of Figures

1.1	Representation of discretizations of the states and band gap tuning in quantum dots	15
1.2	Optical processes in QDs' applications	16
1.3	Colloidal QDs and hot injection	17
1.4	TEM images of HgTe nanocrystals, respectively a) 2.5k, b) 6k	18
1.5	Representation of QDs with ligands, and their action as a tunneling barrier, before	
		19
1.6		20
1.7	<u> </u>	22
1.8	~ · · · · ·	23
1.9	Colloidal QDs solution, functionalized CMOS device using it, SWIR picture taken	
		24
1.10	a)Optical microscope image of interdigitated electrodes, b) electrolyte gated FET	
	with HgTe QDs channel, c) scheme of the functioning of said FET: in gold the	
		25
1.11	Characterization measurements performed on HgTe 6k sample: a) I-V curve and	
	- ,	26
1.12		27
		29
	Inelastic mean free path of electrons in different materials and under different	
		30
1.15	Example of photoemission peaks, taken with Al source in the lab set-up, on HgTe	
		31
1.16	Valence band example on HgTe 6k QDs sample	33
1.17	Cut off example on HgTe 6k QDs sample	34
		35
2.1	${ m HgTe}$ survey taken with Al source. Highlighted in green is the energy of the O 1 s	
	(),	38
2.2	Different angles and components of the XPS machine in use	39
2.3		40
2.4	1, 0 0 v	41
2.5	Fitted peaks example	43
3.1	Band diagram for different QDs sizes. The QDs used in this report are highlighted	
	v i	46
3.2	Surveys and Hg 4f core levels , presented in article [39], before and after potassium	
	deposition	47

3.3	Cut offs taken on 6k samples at different deposition times, and plot of the work	40
0.4		48
3.4	Photo of the deposition process in the preparation chamber, with a sample mounted	40
0 -		49
3.5	XPS surveys of HgTe 6k QDs, pristine and after Cs depositions	50
3.6	Cs 3d core levels: a) after 3 minutes of Cs deposition and b) after 6 minutes Cs	- 1
0.7	deposition	51
3.7	Comparison of the Te 3d and Te 4d core levels before and after Cs depositions .	52
3.8	Comparison of the Hg 4f core level before and after Cs depositions, and fit high-	
	lighting the two contributions of the spectrum (Hg-S contribution is progressively	۲0
2.0	diminishing with the depositions)	52
3.9	Comparison of the top of the valence band before and after the 2 Cs deposition.	55
	Comparison of the cut off before and after the two Cesium depositions	56
3.11	a) Plot of all the work function value with respect to K/Hg, adapted from [39] and b) Plot of all the work function value with respect to Cs/Hg	56
9 19	Band diagrams in function of deposition time	57
3.12	band diagrams in function of deposition time	97
4.1	Variation of the band gap of different QDs in temperature	60
4.2	Effect of temperature on the Band dispersion, as calculated in [57]	61
4.3	Initial survey, taken on room temperature 6k sample	62
4.4	Variation of the 6k core levels with temperatures	63
4.5	Superimposition of Te 4d peaks at room temperature and -100°C (shifted), that	
	allows to see the variation in FWHM with T	64
4.6	Shift of 6k peaks with respect to the temperature	64
4.7	Variation of the 6k valence band with temperatures	65
4.8	Variation of the 6k cut off with temperatures	65
4.9	Fermi Level spectrum captured on Au on Si substrate at room temperature and at	
		66
4.10	Variation of the 4k core levels with temperatures:a), b), and c) are zooms of the	
	= , , ,	67
4.11	Variation of the 3k core levels with temperatures: a), b), and c) are zooms of the	
	Low E_B feature of Hg 4f, Te 4d, and Te 3d	67
	Variation of the 4k cut off with temperature and work function values plot	68
	Variation of the 3k cut off with temperature and work function values plot	68
	Measurements at room temperature taken before and after cooling	69
	Shifts of the Hg 4f core level in temperature for all the sizes considered	70
	Shifts of the Te 4d core level in temperature for all the sizes considered	70
	Shifts of the Te 3d core level in temperature for all the sizes considered	71
	ı v	71
		73
4.20	Curve of 3 k based transistor a) at around -100°C and b)at -30°C. Adapted from supporting information of [59]	74
4 91	Shift of the work function in temperature for all the ODs sizes considered	74 75

Acronyms

Conduction Band

CB

```
\mathbf{CQDs}
      Colloidal Quantum Dots
DOS
      Density Of States
\mathbf{FWHM}
      Full Width at Half Maximum
HAXPES
      \operatorname{Hard} X-ray PhotoEmission Spectroscopy
IMFP
      Inelastic Mean Free Path
\mathbf{IR}
      InfraRed
\mathbf{QDs}
      Quantum Dots
\mathbf{UPS}
      {\bf Ultraviolet\ Photoemission\ Spectroscopy}
\mathbf{TEM}
      Transmission Electron Microscopy
UHV
      Ultra High Vacuum
```

VB

Valence Band

VBM

Valence Band Maximum

XPS

X-ray Photoemission Spectroscopy

Chapter 1

Introduction

1.1 The laboratory and the OCN group

The Optoelectronics of Confined Nanomaterials (OCN) group at the Institut des Nanosciences de Paris (INSP) has its main focus on improving the knowledge on nanomaterials, particularly Quantum dots and 2D materials, and their applications for optoelectronic devices.

Research on the topic is conducted following an interdisciplinary and start-to-finish approach, from the chemical synthesis to the optoelectronic device fabrication and characterization. A variety of both facilities and expertise makes this possible. This will be a non-exhaustive description, limited to what has been most relevant to my experience. A chemistry lab provides the environment for the synthesis of the nanomaterials, devices can be then fabricated in the INSP cleanroom. For controlled environment processes and storages, two gloveboxes are in use. Then a variety of characterizations equipment is present: electronic setups for electrical measurement, 2 cryostats, 2 Fourier transform infrared spectroscopy (FTIR), a Raman spectroscopy set-up, and a X-ray photemission spectroscopy (XPS) analyzer.

1.2 Colloidal Quantum Dots

1.2.1 Quantum confinement

Quantum confinement is the defining effect for nanostructures. It concerns a variety of structures, such as quantum wires, quantum wells and the quantum dots that are the main concern of this work. It consists in the modification of the density of states allowed to the material, that become quantized.

It is a phenomenon that onsets when the size of the structure in one or more dimensions goes below a specific quantity, the Bohr radius, defined as following:

$$a_0 = \frac{4\pi\epsilon_0\epsilon_r\hbar}{m *_r e^2} \tag{1.1}$$

Where ϵ_r is the relative dielectric permittivity of the material, and $m*_r$ is the reduced mass, equivalent to the $m*_r^{-1} = m*_e^{-1} + m*_h^{-1}$, from the effective masses of electrons and holes. As a result, the Bohr radius becomes a material-specific quantity, making the choice of a material that exhibits proper quantum confinement a fundamental step. For sake of illustration, in CdSe the Bohr radius is 7 nm, [1], in PbS it is 21 nm[2], in HgTe is 40 nm [3], so a relevant variation of these values is possible, while still always speaking of nanometer sized structures.

When a material dimension falls below the Bohr radius, its properties deviate significantly from the bulk behavior. For instance, the emission wavelength becomes tunable and no longer solely dependent on the intrinsic material properties, as will be further discussed in the case of quantum dots. Similarly, transport properties can exhibit quantized conductance, as observed in quantum wires.

These effects arise from the discretization of the density of states (DOS), which is continuous in bulk materials but becomes quantized in one or more spatial directions depending on the dimensionality of the quantum confinement. As a result, each class (quantum wells, quantum wires, quantum dots...) of quantum-confined material exhibits a distinct DOS profile and correspondingly different physical phenomena. A detailed discussion of all types would be out of the scope of this master thesis, and only effects on the object of this study, quantum dots, will be presented.

Quantum Dots

A quantum dot is a semiconductor nanoparticle that confines the carriers in all three dimensions, because all of its dimensions are smaller than the Bohr radius. This gives rise to a relevant variation in the DOS, that become both discretized and tunable. Quantum dots are also called nanocrystals, because they maintain crystalline properties even at their reduced size.

A useful way to model the variation in the DOS due to quantum confinement in QDs is through the simple particle-in-a-box model, which assumes that the quantum dot can be approximated as a spherical particle

Suitable starting materials are semiconductors, i. e., a material with an intermediate band gap (between 0.5 eV and 3 eV), with a direct band gap, which means that the top of the valence band is in direct correspondence in the k space with the bottom of the conduction band. The distribution of valence and conduction band can thus be approximated by using parabolic dispersion relations in k:

$$E_{VB} = -\frac{\hbar^2 k^2}{2m_{h}}, \ E_{CB} = E_G + \frac{\hbar^2 k^2}{2m_{e}}$$
 (1.2)

where $m*_h$, $m*_e$ are the effective mass of holes and electrons and E_G is the band gap. This model implies that an electron must overcome a minimum energy, equal to the band gap, to transition from the valence band to the conduction band. In bulk materials, the allowed energy states

form a continuous distribution in k-space. When confinement comes into play, these continuous states are substituted by discretized states, allowing only specific quantized energy values. This transition from continuous to quantized states is represented in figure 1.1.

In the particle-in-a-box model the solution of the Schrödinger equation yields quantized states described by the following expression [4]:

$$E_{n,l} = \frac{\hbar^2 \phi_{n,l}^2}{2R^2 m^*} \tag{1.3}$$

where $\phi_{n,l}$ is the wave function coefficient, depending on the quantum numbers n and l, R is the QD radius, m* is the reduced mass. The exact value of $\phi_{n,l}^2$ is finite and determined by boundary conditions. A complete derivation and treatment of this value is outside the scope of this report. Since the primary goal is calculating the band gap value, is sufficient to consider the first electron and hole allowed level, corresponding to the ground state. These energy levels are given by:

$$E_{1,0} = \frac{\hbar^2 \pi^2}{2R^2 m^*} \tag{1.4}$$

And thus:

$$E_G = E_{G,bulk} + \frac{\hbar^2 \pi^2}{2m *_e R^2} + \frac{\hbar^2 \pi^2}{2m *_h R^2} = E_{G,bulk} + \frac{\hbar^2 \pi^2}{2m *_r R^2}$$
(1.5)

This additional term, often referred to as the quantum confinement term, depends inversely on the square of the quantum dot radius R ($\frac{1}{R^2}$), and is responsible for the tunability of the band gap. As the size decreases, the quantum confinement energy decreases. Smaller QDs are going to have a bigger deviation from the bulk band gap and a bigger band gap in general, as shown in figure 1.1b).

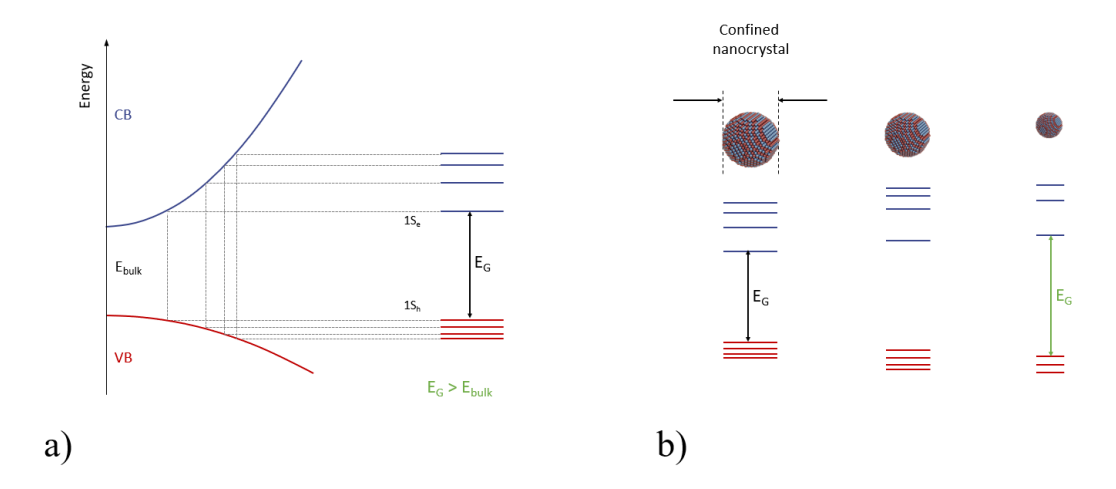


Figure 1.1: Representation of discretizations of the states and band gap tuning in quantum dots. a) Allowed electronic states for a bulk material, following the approximations of parabolic bands dispersion, and for a quantum dot. b) Band gap tuning for different QDs sizes

QDs in optoelectronics: down-converters, LED, Photodetectors

Owing to their size-dependent tunable band gap and to their sharp emission at specific energies (and thus frequencies), quantum dots (QDs) have found significant applications in the field of

optoelectronics. The three main processes that are currently exploited are: photoluminescence, electroluminescence, and conversion of light into an electrical signal (fig 1.2).

Photoluminescence is involved in one of most well known industrial application of QDs: displays. In this case, the quantum dots act as a down-converter, so they emit either red or green light, excited by a blue backlight. This configuration enables the generation of very high quality primary colors pixels, thanks to the aforementionedd QDs bright emission and very narrow spectrum [5]. Electroluminescence, the emission of photons generatede by electrical injection, is also an extensively investigated mechanism. LED based on QDs are very promising in a variety of applications, due to their brightness and tunability of wavelengths[6].

Finally, incident light can excite electrons from the valence to the conduction band, thus generating an electrical signal. This photoresponse can be used either for power generation, as in photovoltaic device, or for light detection. In the context of this study, the focus lies on using QDs for photodetection, where light modulates the current flowing through a device.

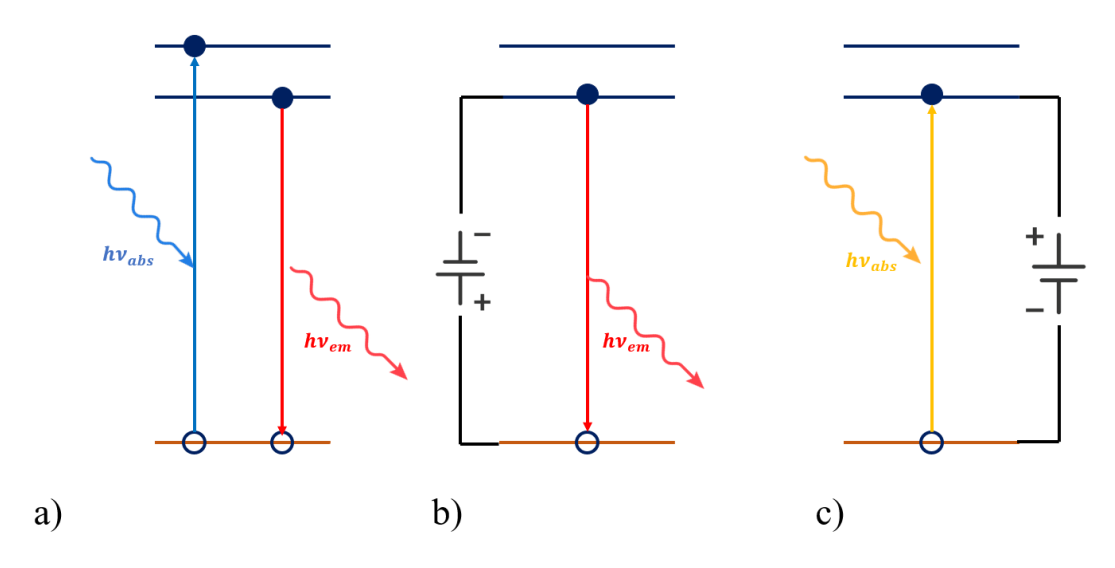


Figure 1.2: Optical processes in QDs' applications: a)photoluminescence for down-converter, b) electroluminescence for LEDs, c) photon conversion in photodetectors

1.2.2 Colloidal quantum dots

Colloidal quantum dots, as the ones used in this report, are solution-processed quantum dots, synthesized and stabilized in a liquid medium. This approach offer a lot of advantages with respect to others techniques, such as epitaxial methods, especially in term of scalability and lower costs.

First attempts to synthesize quantum dots as colloids were reported in the 80s, with foundational works done by Ekimov, Henglein or Brus and their respective groups. The greater advancement for the QDs considered in this report will come in the 19990s. In 1993, Murray, Norris and Bawendi describe the "hot injection method" [7], that allows to obtain monodisperse nanocrystals of cadmium-calchogenides compounds (CdE, where E is either S, sulfur, Se, selenium or Te, tellurium). This work will earn Bawendi, alongside with Brus[8] and Ekimov[9], pioneers of the Quantum dots research in their own, separate, groups, the 2023 Nobel prize in chemistry.

Hot injection synthesis

The method consists of three main steps:

- in a three neck flask, quantum dots precursors (either the cations or the anions), ligands, long hydrocarbon molecule with a functional group that binds to the QD surface, and an high boiling point coordinating solvent, are mixed. Then the mixture is degassed, *i. e.*, brought under vacuum at elevated temperature so that any impurity, and especially oxygen and water, is eliminated from it.
- the mixture is heated to reaction temperature, and the other QDs precursors (either anion or cation), are rapidly injected (equipment shown in figure 1.3). This starts the nucleation of the particles, which terminates very soon due to the drop of the temperatures and the dilution of reagents caused by the introduction of room temperature precursors. From these seeds, the nanocrystals will slowly grow in the solvent. The final size of them depends on factors such as temperature, duration of the reaction and type and quantity ligands present.
- the reaction is quenched. The most used method consist in adding an excess of ligands, to stop aggregation of precursors to quantum dots, and quickly cooling the flask.

Ligands are a defining feature of colloidal quantum dots, as they provide colloidal stability by preventing aggregation and act as surface passivators. The different ligands option play a fundamental role in improving the electronic transport properties in subsequent device applications. Fine-tuning this process allowed to obtain a variety of quantum dots shapes, not limiting to the spherical QD. Different shapes and sizes will create, as anticipated in the section 1.2.1, different photon absorption (figure b in 1.3). A transmission electron microscopy (TEM) image of synthesized HgTe quantum dots (which will be one of the main topic of this report) is provided in figure 1.4. The term 2.5k and 6k refers to the position of the absorption band edge, at 2500 cm^{-1} , $6000 \ cm^{-1}$, respectively

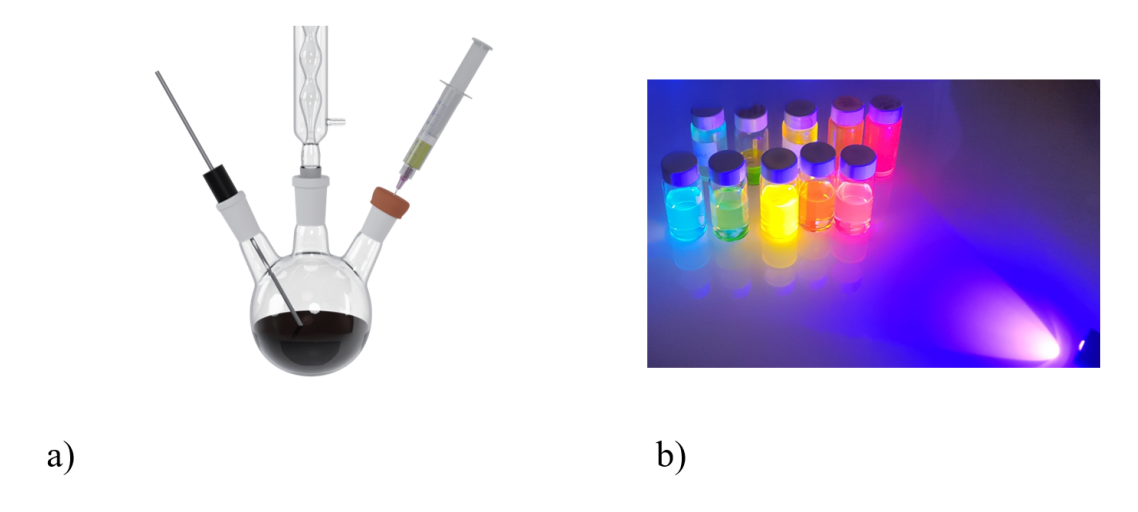


Figure 1.3: a) Three neck flask, thermometer and syringe as used in the hot injection process b) different colloidal QDs, shining under UV light.

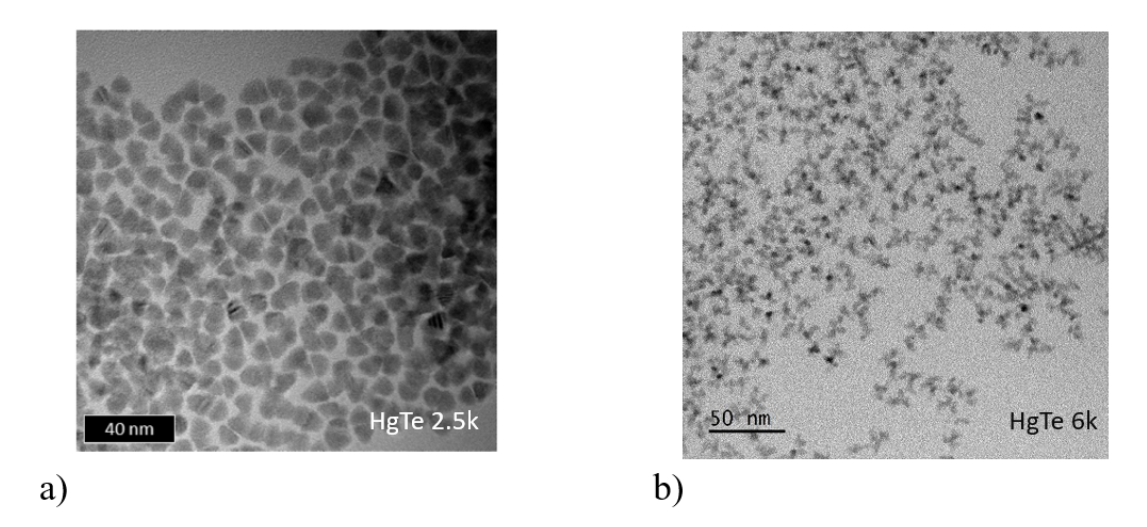


Figure 1.4: TEM images of HgTe nanocrystals, respectively a) 2.5k, b) 6k

Hopping transport in colloidal quantum transport

In all QDs films, transport cannot be a free and continuous movement of the electrons, due to confinement. It configures instead as an hopping process from one QDs to another. In CQDs, the transport is heavily dependent on presence, nature and length of the ligands. The movement from a CQD to the next configures as a tunneling event, due to the high energy barrier that needs to be overcome. By modeling the ligands impediment as a potential barrier, we have:

$$T \approx \exp\left(-2l\sqrt{\frac{2m(V_0)}{\hbar^2}}\right) = e^{-\beta l}$$
 (1.6)

where: T is the Tunneling probability, l is the width of the potential barrier, and thus the length of the ligands, V_0 is the height of the potential barrier, m is the mass of the particle tunneling, in this case, the reduced mass of the electron. This gives an evident correlation between the length of the ligands and the transport behavior in the film. To have an optimal conduction for the desired application, longer ligands, that are better for preventing aggregations, are exchanged with shorter ones, in a ligand-exchange process.

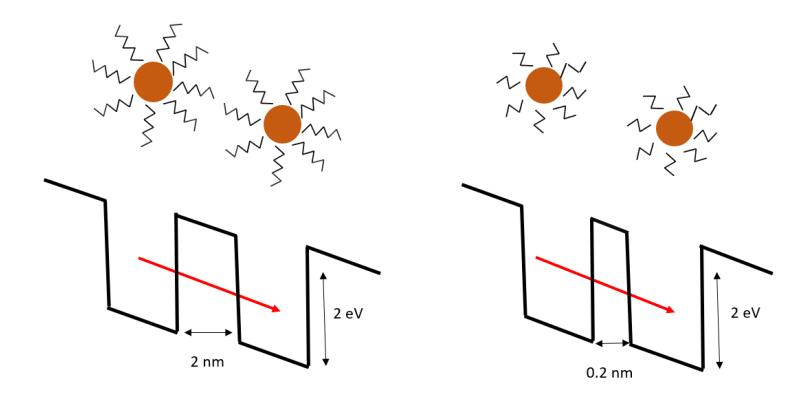


Figure 1.5: Representation of QDs with ligands, and their action as a tunneling barrier, before and after ligands exchange

1.3 Mercury telluride Quantum dots and their use in the infrared range

1.3.1 Infrared range and QDs

Due to their tunability, HgTe quantum dots exhibit strong potential of applications in the infrared, the range in which they present photoluminescence.

The IR spectrum spans from wavelengths longer than visible red light, so from 800 nm and frequencies in the order of 10^{-14} Hz (photon energy 1.55 eV, wavenumber 12500 cm⁻¹) until the THz range, that starts around 3 THz (wavelength= 100 μ m, wavenumber 100 cm⁻¹, photon energy 0.0124 eV). This broad range can then be subdivided into different partitions, following the possible applications domains.

- near-infrared (NIR), is the range between visible light and wavelengths of 1μ m. Easier to study, because CMOS and other technologies for visible light sensing are still able to reach the range, due to silicon band gap being 1.12 eV. Used in facial recognition systems, and active imaging systems, such as night vision.
- short-wave infrared (SWIR), encompasses the telecommunication windows, due to the compatibility with fiber optics. It is still very interesting for imaging purpose, but is not CMOS-compatible anymore.
- mid-wave infrared (MWIR), the possibility of thermal detection starts to onset. Plank equation prescribes in fact that there is a correlation between the emission wavelength of the radiating black body and its temperature:

$$B(\lambda, T) = \frac{2hc^2}{\lambda^5} \cdot \frac{1}{\exp\left(\frac{hc}{\lambda k_B T}\right) - 1}$$

where $B(\lambda, T)$ is the spectral radiance, λ is the wavelength, T is the absolute temperature, h is Planck's constant, c is the speed of light, and k_B is the Boltzmann constant. Wien's displacement law provides a more direct relation between the peak of spectral radiance and

the temperature as:

$$\lambda_{peak} = \frac{b}{T} \tag{1.7}$$

where b, Wiens displacement constant, is around 2898 μ ·K. This gives a wavelength of around 7 μ m for a body at 150°C, so hot bodies emit in the MIR range.

Additionally, and maybe more importantly from an application point of view, these wavelengths are not scattered relevantly by dust and fog, making them particularly appropriate for defense sensing.

• long-wave infrared (LWIR) is the range in which ambient temperatures bodies emit black-body radiation (a body at 25°C peak emission is around 9.72 μm), so it is appropriate to image them. Moreover, it is still widely used in defense.

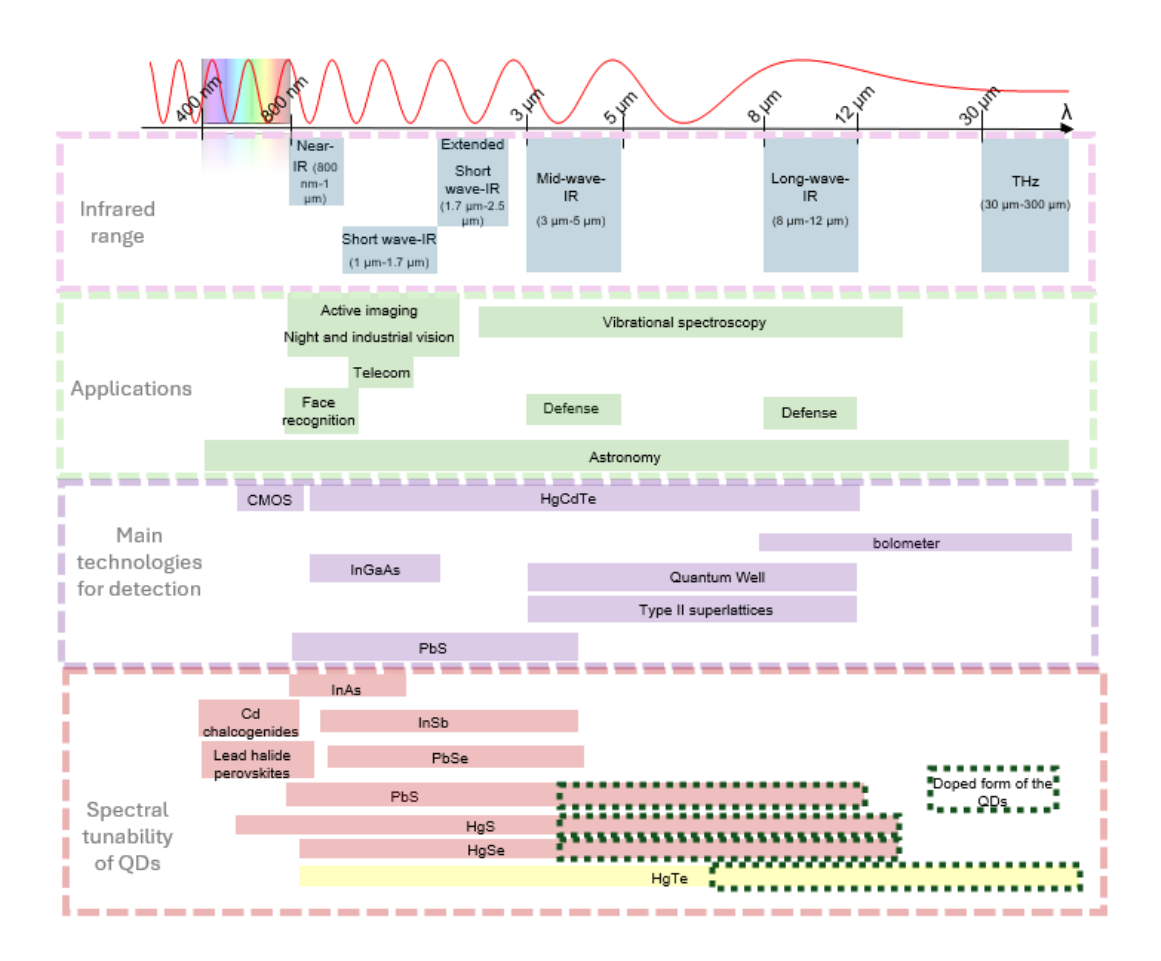


Figure 1.6: Electromagnetic spectrum highlighting the different parts of the infrared range, and correlating applications and main technologies for sensing with tunability range of QDs. Adapted from [10]

Quantum dots are not obviously the only possibility to sense in the IR spectrum, but are very interesting due to the tunability of their range and the possibility of covering a wide range of

applications. Various starting materials can be used: other calchogenides compounds, such as cadmium calchogenides, lead compounds, such as PbS, another material used in the OCN group, and finally mercury telluride, who has a noticeably broad range.

They have, in fact, the broadest tunability due to the specific nature of the band structure of the bulk and to the characteristics of the quantized levels of the QDs. This makes them a very important candidates for optoelectronics.

However, they share the same drawback as nearly all other QDs options operating in the infrared range. Most of these options contain either lead, cadmium or mercury, so most of the compounds here presented are rather toxic and polluting. Moreover, lead, cadmium and mercury are the first three elements noted on the list of restricted materials presented by the Restriction of Hazardous Substances in Electrical and Electronic Equipment (RoHS)[11] directive of European Union, because of their toxic and polluting nature, and a general effort should be made in restricting them. However, it still seems impossible to substitute them. In fact, only Indium compounds are more RoHS compliant and thus promising in that sense, but their range is rather limited, as evidenced in figure 1.6.

1.3.2 Mercury telluride: properties, band structure and relevance for quantum dots

Main object of study in this report's chapter 3 and 4 is mercury telluride (HgTe) quantum dots. Bulk HgTe is a semimetal, i.~e., a material where valence band and conduction band come into contact without crossing over, intermediate case between a metal and a semiconductor. This happens, as more precisely shown in picture 1.7, at the high symmetry Γ point of the Brillouin zone.

A clarification on the definition of the band gap is due: the optical band gap of HgTe can always be treated as zero , but is often reported that HgTe has a negative band gap. This is absolutely true if the band gap is defined as the distance between the states that forms the conduction band and the ones that form the valence band. In fact, the Γ_6 bands, that have an s-like character and form the conduction band, are below the Γ_8 , p-like, bands of the valence band. This is due to the fact that the conduction bands states are a lot more disperse, and end up crossing over the valence bands values. However, the highest occupied states and the lowest unoccupied states touch at Γ point(k=0), even if these all belong to Γ_8 bands, and so the effective energy gap value is 0.

The zero-optical band gap is particularly interesting because it means that HgTe-based materials can have their band gap engineered without a lower bound. One mature option of tunable band gap is the use of HgCdTe alloys, where the Cd concentration directly controls the band gap. IR detectors based on these alloys have been explored since the 1960s and are still used nowadays due to their high versatility[12].

However, HgTe QDs offer equivalent tuning properties, if not finer. From the simple equation reported in chapter one, it is evident how in QDs with a $E_{G,bulk} = 0$, the band gap is solely dependent on the confinement term. This makes HgTe QDs particularly apt for infrared sensing, allowing the possibility of reaching far into the long wave infrared [10].

It is also evident that the shapes of conduction and valence band are relevantly different, and so the effective masses of electron and holes present a discrepancy. The electron effective mass is in fact particularly low, 0.013 times the electron mass[3]; and in contrast, hole effective mass, correlated to the great flatness of the bands, is $0.3m_0$. As an example, in Si $m*^e$ is 1.08, in Ge it is 0.12, and in another semiconductor of the same group of HgTe, CdSe, $m*^e$ is 0.18. This is another reason why HgTe is such an optimal material for quantum confinement of electrons, and thus for realizing QDs, because the already mentioned Bohr radius is particularly large, creating

a strong quantum confinement.

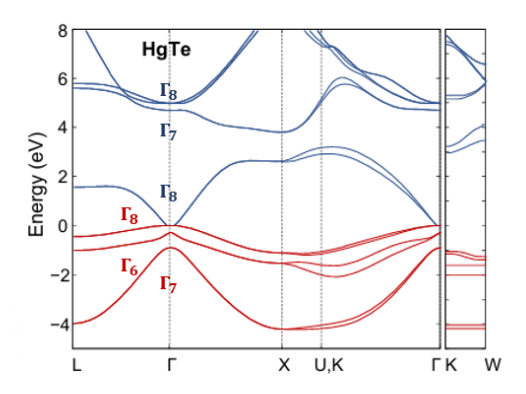


Figure 1.7: Full electronic band structure of bulk HgTe, adapted from ref [13]

Another interesting feature that is already evident from figure 1.7 is the presence of a non-parabolic linear dispersion of the bands, which is correlated to relevant differences in the scaling of the confinement term, which is more close to R^{-1} than to R^{-2} .

1.3.3 Inter and intraband transitions in HgTe QDs

HgTe QDs present one of the broader spectral tunability, going from the NIR to the Thz. The large range of absorption, and eventually emission, wavelengths do not come only from the band gap tunability. In fact, the absorption in this range is not necessarily happening only in the tuned band gap of these quantum dots, so as inter band transitions, from the highest level of the valence band to the lowest level of the conduction band. An important contribution is given by the intraband transitions, so the ones that happen in the quantized band states coming from the conduction band. This process is mainly in the conduction band because of the more disperse and less flat shapes of the original bands in bulk HgTe, and mostly limited to the first and second state, such as 1 S_e and 1 P_e (due to filling of the levels and excitation energy). These have a smaller difference in energy than 1 S_e and 1 S_h , and thus are reaching longer wavelengths, as shown in the absorption spectra in figure 1.8.

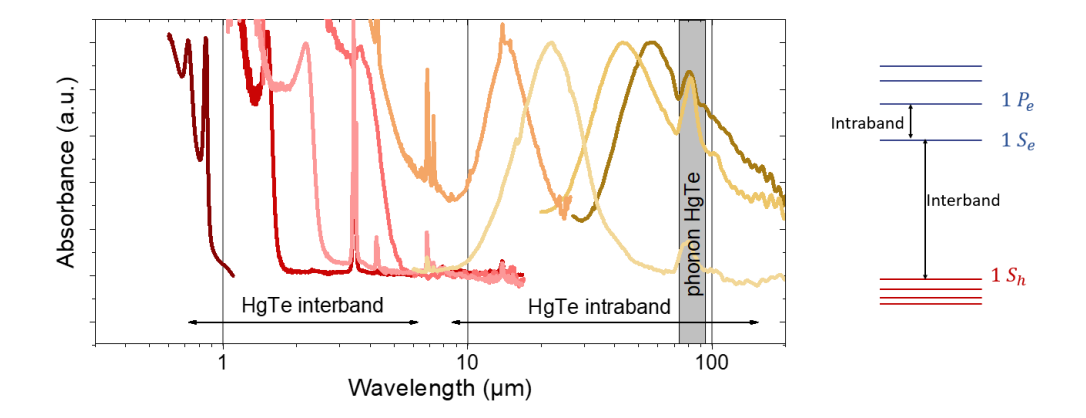


Figure 1.8: Spectral range of HgTe nanocrystal, and inter-intraband transition scheme

More consideration on the behaviour of HgTe at low temperature and the possibility of doping HgTe will be discussed in chapter 3 and 4, along with the experimental work done on that topic. Other than its specific band structure, HgTe QDs present advantages due to the relatively high stability in air of the material, especially compared to other promising material for QDs in the same spectral range, such as III-V semiconductors[14]. Neither of the two main component, mercury and telluride, is prone to oxidation in atmospheric conditions, actually Hg is particularly resistant to that. The limiting factor for the use of these CQDs in air would come from the ligands, that are more prone to air degradation[15].

All this qualities allowed HgTe QDs to come to the rise as important components for infrared optoelectronics.

1.3.4 Mercury telluride quantum dots: story and applications

Another strength of mercury telluride quantum dots is their long story. HgTe colloidal quantum dots are first obtained in 1993 by M. Müllenborn's group[16], but their infrared properties are not reported. 6 years after, A. Rogach group will report the first stable and presenting IR properties HgTe CQDs, really starting the interest of researchers in the topic[17]. Other groups will continue to contribute to the study, as the one of H. Kim, which will provide great advancement in the electrical transport[18], and then, in 2006, report the first photodetector with response to 1.6 μm . In the same year, also important advancement on the synthesis side are made by M. Kovalenko et al.[19], that obtains the synthesis in organic solvents, and the smaller band gap, thus the reddest photoemission. In the 2010s, further results for detector in the MWIR and SWIR range are obtained, and another breakthrough will come in 2016, with the realization of nanoplatelets, with the cation exchange method from the group of S. Ithurria [20], leading to important results in the field of emitters. From then on, also thermal detector applications[21] and LED start to be reported, importantly crossing the 2 μm emission [22]. Overall, this confirms them as a very important presence in the infrared field.

One of the most exploited sides of mercury telluride quantum dots is in photodetection. Both photoconductors (where the change in conductivity due to illumination is measured) and photodiodes (diodes in which photon generated carriers appears and are then separated, generating electrical effects) are widely reported in literature. First photoconductive detector is reported in 2006, in the

SWIR range, while the MWIR is reached few years later, in Philippe Guyot-Sionnest's team[23]. Phototransistor also appears, transistors where the channel is created in the QDs films. Differently from photoconductors, where light directly changes the material's conductivity, phototransistors use the generated photocarriers to modulate the current through a separate channel, providing built-in signal amplification.

The use of photodetectors based on HgTe nanocrystal are not limited to single pixel, in fact, their device integration is rather mature: Focal Plane Arrays (FPAs) are reported[24], and pictured in figure 1.9 there is one of them, constructed in the lab[25].

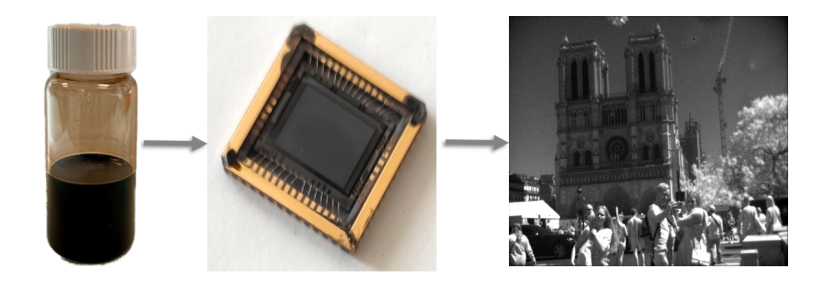


Figure 1.9: Colloidal QDs solution, functionalized CMOS device using it, SWIR picture taken with it.

The facility of integration of the colloidal QDs, which can be simply spin coated on the circuitry, and the extremely large range of spectral tunability makes them a particularly interesting alternative against the more used counterparts, such as HgCdTe detectors, that for example present a smaller absortion range (see also fig 1.6).

1.3.5 HgTe based photoconductors

One of the most reported use of HgTe Nanocrystals concerned in our study is as photoresponsive conduction layer, to operate either as photoconduction layer or as a simple transport layer in transistors. Here described are the steps for fabrication and characterization as performed in the lab.

Fabrication

All the fabrication steps here discussed are realized into INSP clean room, so they are in the hand of the group from start to finish. Different substrates are used as a starting base for transistors, such as glass, Si and $\rm SiO_2$ wafers, evaporators are available for depositing metals, photolitography can be done either through optical photolythography set-ups, through masks designed by the team, or e-beam. As an example, here it will be reported the fabrication process for gold interdigitated electrodes on glass.

The design of interdigitated electrodes has the twofold objective of increasing the contact area between the electrodes and the quantum dots film, and have a particularly short channel, which allows for faster transport and lower operating voltages.

Starting substrates are microscope glass slides, cleaned with acetone, then isopropanol, to remove dust and organic residues, and then subsequently plasma cleaned with oxigen plasma, to promote adhesion and eliminate all the eventual residues (of contaminants and solvents used to clean).

Then both primer and sequentially resist are spin coated on. Lithography is then performed, specifically with an image reserval resist process: this makes it a two steps lithography process, with a first exposition through the mask, a bake to reverse the resist behavior, and a second flood exposure, an even illumination without the mask. This particular technique allows to have concave edges, appropriate for metal lift-off than would be then performed. The obtained pattern is checked through an optical microscope and a profilometer. An adhesion layer of either Cr or Ti is evaporated, followed by the gold itself. Then, acetone lift-off is performed, and all electrodes are checked electrically.

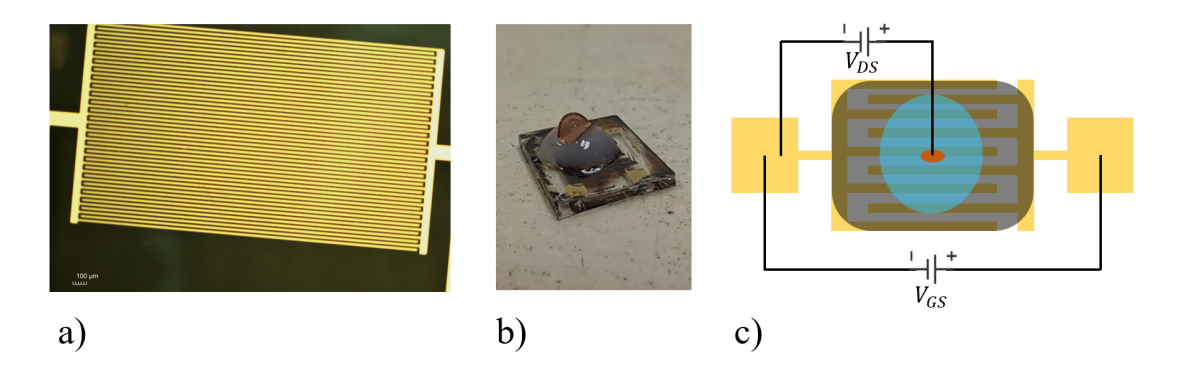


Figure 1.10: a)Optical microscope image of interdigitated electrodes, b) electrolyte gated FET with HgTe QDs channel, c) scheme of the functioning of said FET: in gold the electrodes on the glass substrate, in black the QDs film, in blue the electrolyte

Electrical characterization on FETs

Quantum dots film electrical characterization is often done on devices. These allows, with the use of an electrical characterization station, to quickly derive the behaviour of the film and their gating properties. The aforementioned device in this case consists of a pair of source and drain electrodes, made as interdigitated gold on glass electrodes fabricated as described in the previous section, over which a nanocrystal film is spincoated. From this it is already possible to observe, through bias applications, the typical behavior of the nanocrystal films, that is, as evidenced by the shape, not simply linear which would suggest a purely resistive behavior. In figure 1.11 a) the I-V curve of a device with active layer made of HgTe 6k nanocrystal is shown. The symmetry for positive and negative voltages is to be expected, since until now we are working on symmetrical devices, and on an ambipolar conductive layer. These films are realized with 6k, which is indeed ambipolar (this will be debated later in section 3 and 4). These devices also shows photoconductive behaviour: sudden increase of the current is evident when a blue light is shone on the film.

A more complex 3 terminal device, so with drain, source and gate, can also be realized (figure 1.10). In this case, different gold on glass electrodes, obviously comprising a gate in this case, are used. The film is again spincoated on, but is then removed from the gate area, and then an electrolyte, $LiClO_4$, in an organic matrix, is deposited (in a nitrogen-filled glovebox). Over the electrolyte a copper flake is deposited to ensure again proper contact. Then, on the probe station, 2 voltages are applied: V_{GS} , between the gate and source is scanned, generating the gating effect, while V_{DS} is maintained fixed, to still have current conduction. The mobility of carriers is calculated in the

triode regime, so V_{DS} value is chosen at 0.5 V, to have always $V_{GS} > V_{DS}$ and not induce the saturation regime.

The mobility in the film can be recovered by the following calculation, that is valid for both type of carriers:

$$\mu = \frac{L}{CV_{DS}W}g_m \tag{1.8}$$

Where C is the capacitance of the matrix with the electrolyte, which in this case is $1~\mu F cm^{-2}$, L and W the dimension of the channel and g_m is the slope of the IV curve, taken on the negative voltage side for holes and the positive for electrons, as shown in figure b) 1.11. The mobility of both holes and electrons in the film result to be very similar: around $0.001 \frac{cm^2}{Vs}$, more precisely $\mu_h = 9.6 \times 10^{-3} \frac{cm^2}{Vs}$ and $\mu_e = 9.0 \times 10^{-3} \frac{cm^2}{Vs}$.

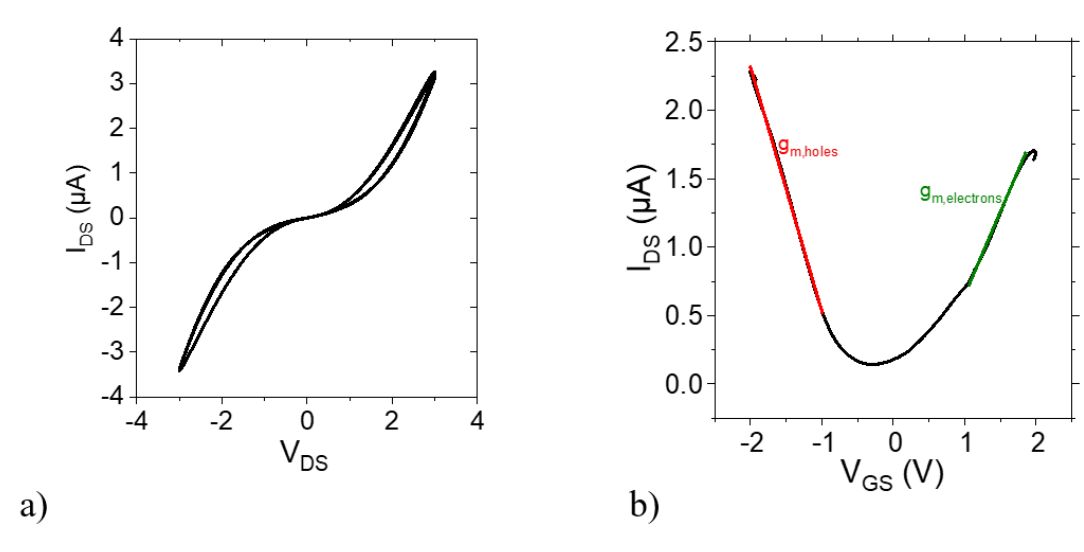


Figure 1.11: Characterization measurements performed on HgTe 6k sample: a) I-V curve and b) transfer curve

1.4 Photoemission: XPS technique and setup

1.4.1 Overview on the basic principle of photoemission spectroscopy

Photoemission spectroscopy is a technique that combines chemical and physical analysis of a material in one single method. It is based on the photoelectric effect, observed first by H. Hertz in 1887 and then explained with the quantum nature of light, by Albert Einstein in 1905. Such effect can be very briefly and non-exhaustively described as the emission of electrons from a material when excited by photons. These electrons have a specific energy, which is correlated to the photons' kinetic energy, the electronic state and other characteristics of the material that can be determined, thus allowing the use of photoemission as a way to probe the occupied electronic states of a specific material. More specifically, the desired sample is irradiated with a monochromatic, high energy (i. e., from several eV to some keV) source of photons. Said photons will interact with the electrons of the material, freeing them to the surface, as shown in figure 1.12.

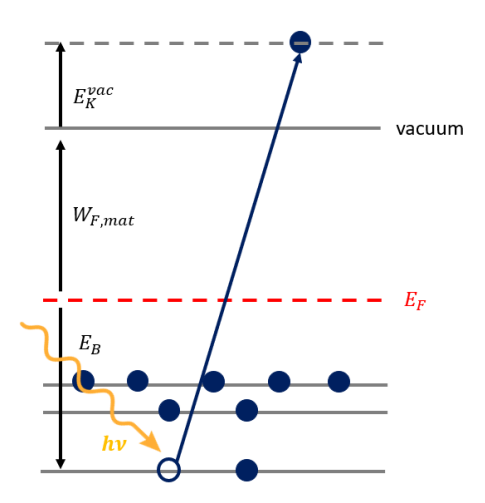


Figure 1.12: Schematic representation of photoemission spectroscopy

The most known model to describe theoretically the photoemission process is the "three steps model" [26]:

- i the electron is optically excited inside the sample
- ii it travels to the surface of the sample
- iii it crosses the surface of the sample and enters the vacuum.

In the first passage, a photon with sufficient energy can be absorbed by an atom, and induce one of the electrons to leave its bound state for a free state inside the sample. The probability of this process is closely related to the photoionization cross-section, that in turn depends on the initial photon energy and on the atom and the orbital shell from which the electron is emitted.

During the photoelectron transport to the surface, the electron can interact with the lattice in different ways. They can either be:

- elastically scattered, and arrive at the surface without suffering energy loss. These electrons will maintain the information on their energy level of provenance, and be identifiable in a photoemission spectra because they will generate peaked and evident emissions.
- inelastically scattered, and lose a moderate amount of the initial energy. These losses could be due to electron-phonon coupling, or electron-electron or electron-plasmon transition. These will still be that they give rise to other feature on the spectrum, such as satellite peaks or peak broadening.
- strongly inelastically scattered, loosing track of their initial energy. These are defined as secondary electrons and create a background signal on the spectrum.
- unable to escape from the surface, due to excessive energy loss. These electrons, as could be expected, do not generate any signal

Finally, the electron at the surface has to overcome the work function, the minimum energy to move an electron from the Fermi Level to the vacuum.

From the energy conservation law, it is possible to describe the energy of the photoemitted, elastically scattered electron, with the following equation:

$$h\nu = E_K^{vac} - E_B - W_{F,mat} \tag{1.9}$$

where E_K^{vac} is the kinetic energy of the excited photo electron, $h\nu$ is the energy of the impinging photons, E_B is the binding energy of the photoelectron and $W_{F,mat}$ is the sample work function. However, the equation here written presents 2 incognita, the work function and the binding energy of the sample. In reality, it is not necessary to known the work function of the sample. During measurements, the sample and the analyzer are in fact grounded to the same ground, and thus have the same Fermi Level (see figure 1.13). The Kinetic Energy measured by the analyzer is then:

$$E_K^A = E_k^{vac} - (W_{F,A} - W_{F,mat}) = h\nu - E_B - W_{F,mat} - (W_{F,A} - W_{F,mat}) = h\nu - E_B - W_{F,A}$$
(1.10)

and thus the electron binding energy can be calculated as

$$E_B = h\nu - E_K^A - W_{F,A} \tag{1.11}$$

without any dependency from the material work function, only to the known analyzer work function.

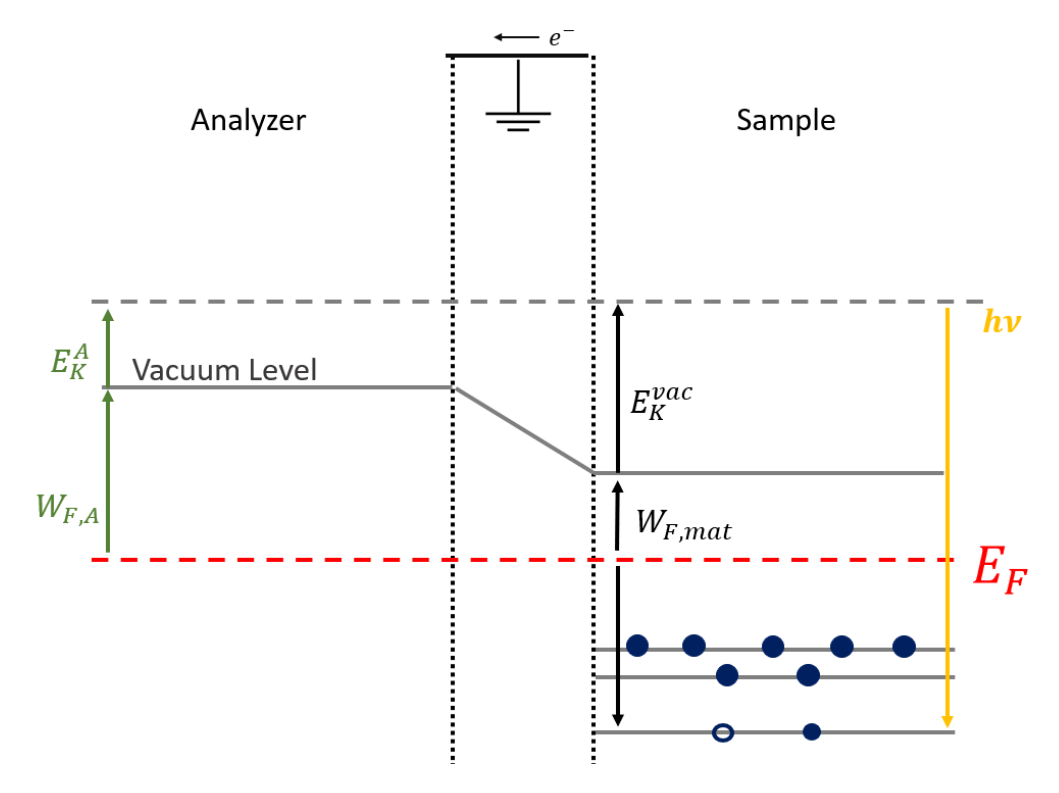


Figure 1.13: Scheme of energy levels during XPS measurements

1.4.2 Sampling depth

Photoemission is a surface technique, that probes a limited thickness, few or few tens of atomic layers. This limitation arises from the requirement that photoelectrons must exit the material without undergoing too much inelastic scattering, rather than from the penetration depth of the source photons. Indeed, the sampling depth is directly related to the inelastic mean free path,(IMFP), of photoelectrons. More specifically the maximum sampling depth is $3\lambda\cos\theta$, where θ is the angle of emission with respect to the surface normal, so at maximum it can be 3 times the effective inelastic mean free path of the electrons.

The IMFP has a dependency on their starting kinetic energy, and thus on the photon energy. This relationship is not linear, but presents a minimum around 50 eV. On a general note, however, an higher starting kinetic energy means a longer IMFP. The IMFP is dependent also on the sample's material itself, so to estimate the the precise position of the atomic layer probed it is necessary to use calculations as the ones presented in figure 1.14. Thi can be used to predict at least generally the sampling depth.

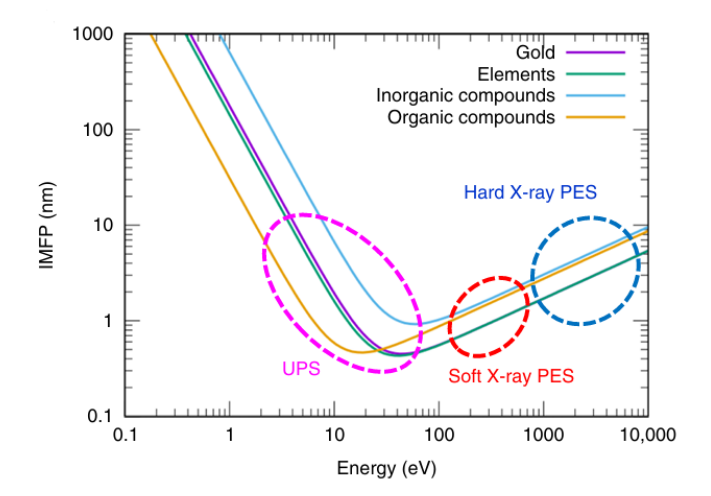


Figure 1.14: Inelastic mean free path of electrons in different materials and under different photon sources, adapted from ref [27]

This figure is particularly important to introduce the different photoemission options. In fact, the energy of photons used can span from the ultraviolet to the hard X-ray spectral ranges. In laboratory set-up, this is obtained from X-ray tubes, where the anodes are made from a specific material and emits photons at the specific wavelength. The sources are thus identified with their material, and the line of the spectrum they produce.

Also, for the electrons to travel undisturbed to the detector, there is the necessity of working in vacuum, or more precisely in UHV, so in the range of 10^{-7} Pa.

The emission of primary and secondary electrons from the sample surface induces a net positive charge accumulation. If this surface charge is not effectively neutralized either by conduction through the sample or by grounding to the measurement apparatus, it results in electrostatic charging of the specimen. This charging manifests as a rigid shift of the measured photoelectron spectra towards higher binding energies, complicating accurate spectral analysis, particularly for insulating or poorly conductive materials. To mitigate this effect, meticulous grounding of the sample to the sample holder is essential. Additionally, charge compensation can be achieved via electron flood guns (neutralizers) that provide low-energy electrons to neutralize the positive surface charge. This tool however needs to be used with cautions, because it could lead to overcompensation risks.

1.4.3 Core levels

The key evidence for the presence of core levels, the electronic shells filled with electrons in the material, comes from distinct features in the photoemission spectrum known as core level peaks. These appear as sharp increases in detected electron intensity at specific binding energies.

Each peak correspond to a specific core shell value, with their own quantum numbers, and is always found at at their specific binding energy. Each core level is going to be identified with the following notation: $El\ nl_j$, where El is the element of provenance, n is the principal quantum number, $(n=1,\ 2,\ 3,\dots)$, while l indicates the orbital angular momentum quantum number, denoted as $s,\ p,\ d,\ f$, corresponding to respectively $l=0,\ 1,\ 2,\dots,\ n-1$. Finally, j is the angular momentum quantum number and is either $j=|l-\frac{1}{2}|$ or $j=|l+\frac{1}{2}|$ depending on whether the

unpaired electron left behind by photoionization has spin vector parallel or anti-parallel to the orbital angular momentum vector [28].

j describes the spin orbit splitting, a crucial phenomenon observed in XPS spectra. Basically, any core level signal coming from an orbital different from s ($l \ge 1$) will present as two peaks, with specific features. These two peaks will have:

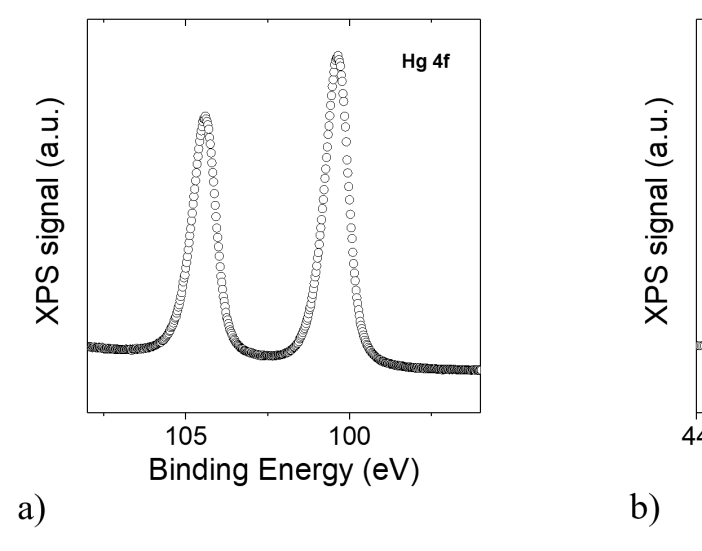
• a precise area ratio, characteristic of the orbital/subshell (p, d, f). This is calculated as the ratio of the degeneracies, which are given by 2j + 1, of the two levels. The values for j and area ratio for each shell are provided in table 1.1.

Table 1.1: Spin-orbit splitting: j values and area ratios for different subshells

Subshell	j values	Area Ratio
s	1/2	n/a
p	1/2, 3/2	1:2
d	3/2, 5/2	2:3
f	5/2, 7/2	3:4

• a defined energy splitting (difference in energy between the two), that is typical of their element and their orbitals of provenance, and thus can be used as a way to identify them.

In figure 1.15, an example of the two most used photoemission peaks studied in the contest of this report is shown, Hg 4f and Te 4d. They present spin orbit splitting of respectivele 4.1 eV and 1.5 eV, and area ratio of 0.75 and 0.67.



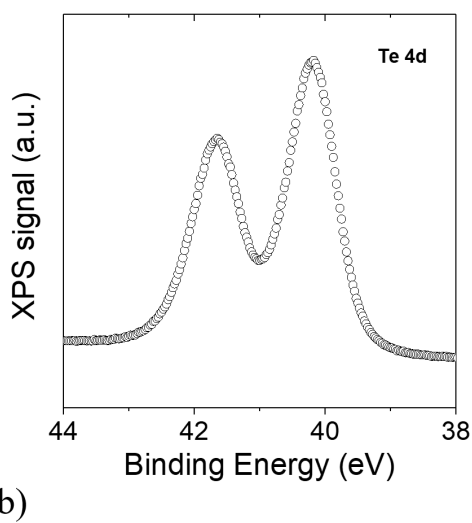


Figure 1.15: Example of photoemission peaks, taken with Al source in the lab set-up, on HgTe 6k QDs. a) Hg 4f photoemission peaks, b) Te 4d photoemission peaks

Chemical shift

Chemical shift refers to a change in binding energy of a core level caused by changes in the chemical environment surrounding the atom.

The energy of photoemission peaks corresponds to the binding energy of their core level of provenance, as prescribed by Koopmans theorem. The value is, in reality, also influenced by the relaxation process that screens the hole after photoionization, but is more or less corresponding to the frozen orbital energy.

Core electrons experience the influenced of their chemical environment, including the Coulomb interaction with the other electron and by the attraction to the nuclei. The chemical environment will influence the distribution of the valence band electrons, that in turn influence the core levels. For example, a diminution of valence electron (thus a more positive charge in the valence band), will cause an increase in binding energy, while an addition of electrons will shift the core levels to lower binding energies. The variation of binding energy results in the shift of the corresponding XPS peak. This change in binding energy of a core electron of an element due to a change in the chemical bonding of that element is called a chemical shift:

$$\Delta \xi = -\Delta \epsilon_i - \Delta E^R + \Delta E_F \tag{1.12}$$

where:

- $\Delta \epsilon_i$ is the variation of the initial state energy, the real chemical shift induced by the bonding of different atoms. Its contribution can be represented with as a simple physical model. We consider a point charge e (which represent the core hole) by the valence charge at a distance r (approximately the distance from the nucleolus). Thanks to the Gauss theorem we have $\Delta \epsilon_i \propto -\frac{Cdq}{r}$, where r is the distance of the core hole from the valence band, and dq is the charge transferred from the initial atom to the other atom in the bond. If dq > 0 the atom is giving charge, because it is binding to a more electronegative atom, and thus the initial state energy decrease and the binding energy of the core level increase.
- ΔE^R is the final state shift, and it the screening capacity of the core-hole by the environment (extra-atomic relaxation). In a solid the extra-atomic relaxation energy is approximated by the electrostatic polarization energy around the hole.
- ΔE_F is the variation of the Fermi Level. The Fermi Level at the surface of a material can be different due to the change of symmetry that varies the band structure, creating for example new gap states which determine the position of the Fermi level at the surface and, subsequently, the band bending.

Calibration of the Fermi level

The spectra hereby shown are all plotted in E_B . In theory, in our case, in which the set-up work function is known, these could be calculated only from equation (1.11). In practice, is often desirable to have a precise, experimental calibration of these values. By definition, at $E_B=0$ is located the Fermi Level of the material. In metals, which do not present a band gap, there is a sharp increase of photoemission at the Fermi level, and this distinct feature can be taken as a reference. So a calibration can be performed by taking XPS spectra of pure (cleaned by sputtering) metals, Au or Ag, and using them as a reference for the Fermi Level.

1.4.4 Determination of Valence Band Maximum and of secondary electron cut off

The core level identification for analysis is not the only important measurement that can be performed in a photoemission analysis: the Valence Band Maximum (VBM) measurement and the Cut Off extraction are also possible options.

The VBM corresponds to the energy difference between the top of the valence band and the Fermi level. It can be estimated by analyzing the onset of the valence band photoemission spectrum at low binding energies. It corresponds to the intersection point between the extrapolated linear slope of the rising edge and the baseline corresponding to zero signal intensity.

In fact, the Fermi level is by definition at $E_B = 0$, and the very first photoemission signal that is in this area of low E_B would come from the electronic state close to it, that is the top of the valence band.

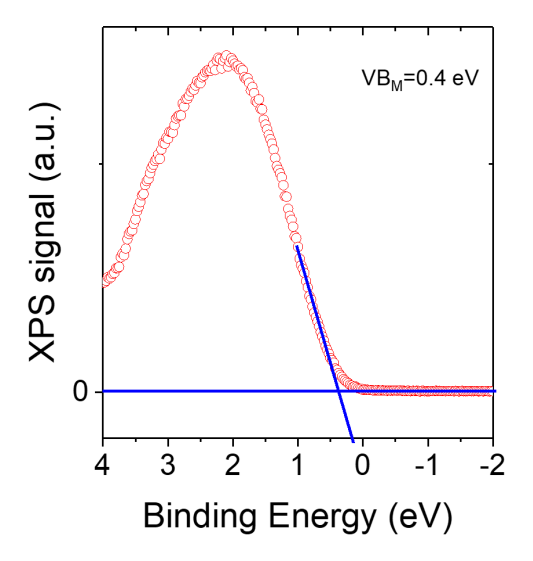


Figure 1.16: Valence band example on HgTe 6k QDs sample

With this method, the error can be defined by taking into account the steepest and flattest lines that still span the linear position of the valence band edge. The largest and smallest value for the valence band difference with the Fermi level are thus extrapolated. From the mean of them, a confidence interval of ± 50 meV is obtained on the measurement.

Also the determination of the work function of the material can be conducted. In this case, the analysis is performed on the secondary electrons, i. e., the electrons that have suffered inelastic collisions, have lost energy during them and do not bear trace of their initial Binding Energy. In particular, the electron of interest in this case have only the energy to overcome the work function of the sample and escape into the vacuum[29]. In this case, to collect these electrons, a bias needs to be applied, in our setup this bias corresponds to -10 V. A sharp diminution(a cut off in fact) appears at Binding Energy close to the $h\nu$ of the photons minus the voltage applied, which corresponds actually to the lowest kinetic energy electrons escaping the surface. The secondary electron cutoff is then identified by identifying the slope of this edge and intersecting it with the baseline (zero-intensity), similarly to the valence band. The work function can then be calculated

from this cut-off value, with the following equation.

$$W_F = h\nu + e \cdot V_a - E_{B,measured} \tag{1.13}$$

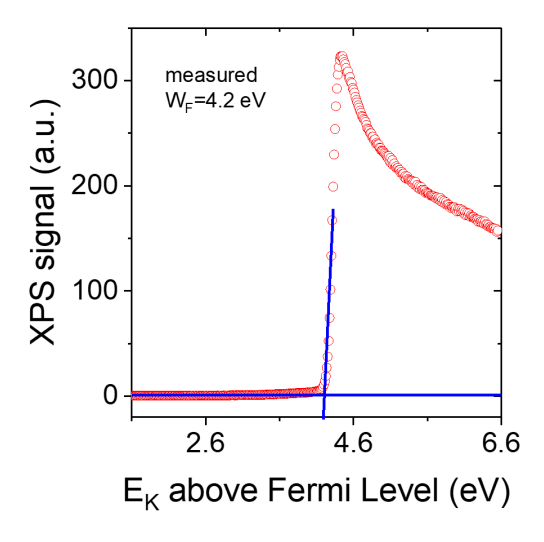


Figure 1.17: Cut off example on HgTe 6k QDs sample

It is possible to use the values of work function and valence band thus obtained in the construction of the band diagram. It is incorrect to affirm, however, that the full spectrum of allowed states can be reconstructed with XPS measurements; photoemission spectroscopy is in fact a technique that only probes filled electronic states, and thus, the position of the bottom of the conduction band cannot be recovered. The band gap however can be measured by other techniques. One option is Fourier-transform infrared spectroscopy (FTIR), which allows to recover the optical band gap. In materials where excitonic energy corrections are negligible, which is HgTe QDs case[30], the optical band gap corresponds well to the electronic one. So, it is possible to draw a band diagram of the material by combining these two techniques, and this is the procedure followed in this report.

1.4.5 X-ray photoemission spectroscopy (XPS) and Hard X-ray photoemission spectroscopy (HAXPES)

As already presented in the previous section, energy conservation prescribes that the photon source is connected to the penetration depth in the material. This creates the fundamental distinction between two techniques such as "conventional" XPS and HAXPES, that differ in the range of the source: around one keV versus a few keV. This first and foremost means that they will probe different layers; XPS is able to recover information until 1 nm while HAXPES can reach the aforementioned tens of nm from the surface.

However, they do not only allow to probe different depths but also to see efficiently different features of a photoemission spectrum.

First of all, an higher probing energy will probe higher binding energies and more deep core levels in the atoms, thus the extension of the surveys are rather different.

Then, there is also the difference in peaks appearance and visibility: in fact, peaks have a different

cross section at different sources, which means that peaks can be almost impossible to see in one source and pretty evident in another. For all this reason, in some cases, the use of both leads to the most complete study. In the set-up in use at INSP, two sources are available in this range: the XPS one, that is an Al $K\alpha$ source of 1486.6 eV and the HAXPES, a Cr $K\alpha$ source, of 5414.8 eV. The stark difference that comes from using one or the other to do a study is evident in figure 1.18

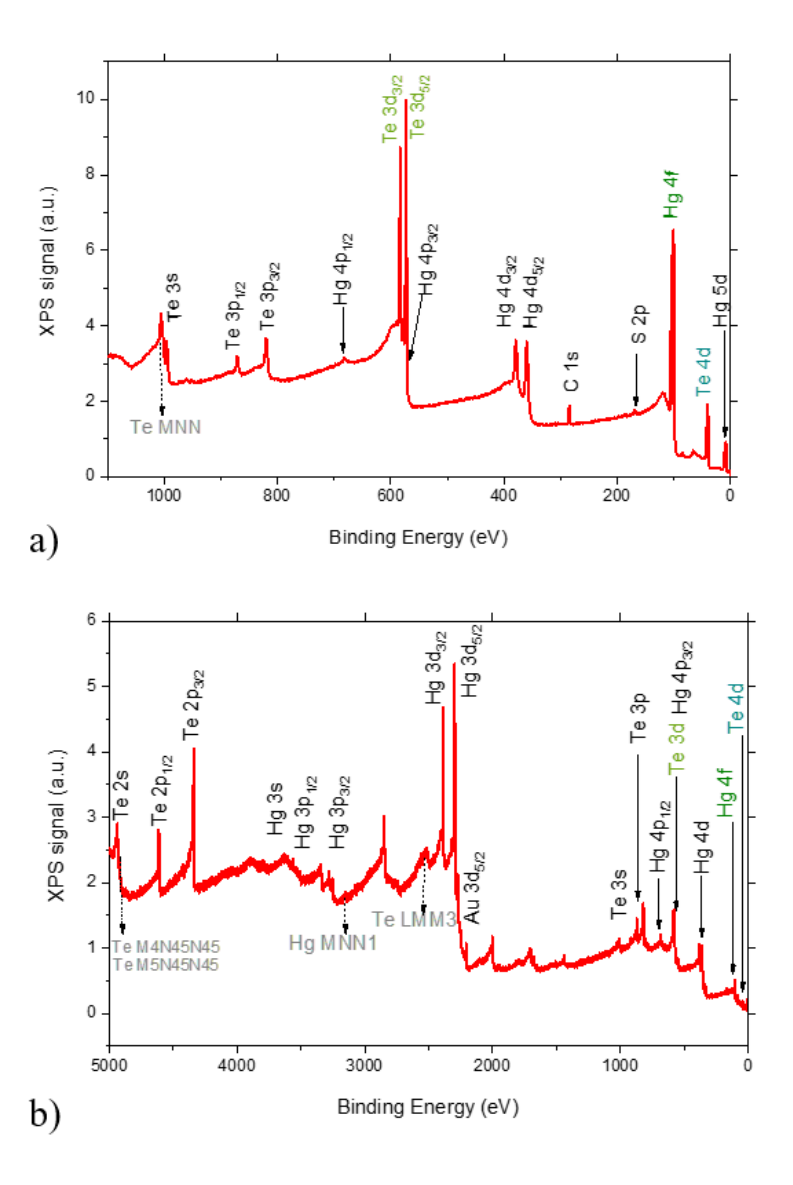


Figure 1.18: Comparison of spectra taken with XPS vs HAXPES. a) is taken with an XPS source, Al 1486.6 eV, b) is taken with an HAXPES source, Cr 5414.8 eV. In green are evidenced the same peaks for each spectra. In grey the Auger photoemission peaks, originated by emission of an Auger electron.

UPS, ultraviolet photoemission spectroscopy

Ultraviolet sources, so with $h\nu$ comprised between 10 and 45 eV, give rise to UPS. A typical source, which will be used also in the lab set-up, is Helium 1 α , 21.22 eV. The use of this particular technique is particularly appropriate to probe the very surface of the material and especially to determine the VBM because it excites, due to the low energy, mainly electrons from it, so the spectrum should be dominated by it.

1.4.6 In situ and Operando concepts.

In situ, XPS measurements refer to experiments conducted on a sample that is modified or processed within the same experimental setup. Example of in situ are measurements performed before and repeated after a desired element has been adsorbed on the surface, or after the sample has been heated or also when the sample is milled. The goal is to study the evolution of the sample and often to analyze one sample in the most realistic conditions, recreating for example its operating environment.

Operando, in photoemission, refers, in the context of this report, to the analysis of a device or one of its layers while it is operating, in conditions that are closer to its realistic operation. The best example would be a device analyzed while the appropriate bias is applied. In fact, photoemission is particularly suited for the analysis of a device, given that it is an ultra high vacuum technique, where the sample, after degassing, remains mostly unchanged, that makes it very appropriate to use, and even more so in the case of photodetecting nanocrystals device, that are typically characterized in a cryostat, under vacuum conditions. It is a concept that has been strongly developed and used in the group in the last year, and one of the very reason of the existence of the XPS set-up. In fact, analysis has been performed on a photodiode, transistor, and FPA [31][32][33].

Chapter 2

Experiments, Materials and Methods

2.1 Samples' preparation

Quantum dots are synthesized in the lab, by chemist engineer Yoann Prado, following Keuleyan's procedure [34]. Different sizes of quantum dots are used in the experimental part of this thesis: they are denominated 6k, 4k, 3k. The naming of them refers to the absorption band edge, respectively $6000 \ cm^{-1}$, $4000 \ cm^{-1}$, $3000 \ cm^{-1}$.

Ligands exchange is a fundamental part of the process that allows to realize high quality conductive films. The properties of the ligands that provide a correct conservation of the QD as colloid are different from the ones desirable for electrical conduction. Longer and thus more insulating ligands are more appropriate to avoid the re-aggregation of the particles, while shorter ones are preferable for the use in films.

For the samples discussed in this report, liquid-phase ligand exchange is used. QDs start dispersed in a non-polar solution, usually toluene. Then they are mixed with a polar solvent containing ions, and due to the nature of the two, a phase separation appears. The top phase will contain the apolar part, in which the longer ligands, detached by the ions, are present, and the bottom the polar, with now the QDs, capped with ions and shorter ligands. Then the QDs can be precipitated and redispersed into a polar solvent, creating a concentrated ink, that then gets directly spin coated on the substrates, allowing the direct realization of films. The detail of this process will depend on the quantum dots taken into account.

HgTe 6k quantum dots are prepared through mixing them in a vial with a liquid exchange solution, comprising of HgCl₂, mercaptoethanol, (MPOH), in DMF, Dimethylformamide. These are then washed with hexane, and then precipitated through centrifugation in toluene. The precipitated quantum dots are dried and then redispersed in DMF. 4k can be made with the same procedure, being particularly careful during the drying procedure to avoid aggregation. 3k quantum dots need to be treated slightly differently, needing at least 2 washing steps and an overall more gentle treatment and strong redispersion.

After that, an ink can be stored for some time in a freezer, in a carefully closed vial. Ink can then be spin-coated. It can be worth it to make some test spin-coating before the process is done, because the different re-dispersion quantities can give rise to different thickness for each ink, even with the same spin coating velocity parameters. This has proven particularly relevant in the context of preparing samples for XPS analysis, where an excessive thickness can lead to an

unimperfect grounding of the film, and the substrates used are characterized, due to the gold presence, by low wettability.

The substrates used for the films analysis with XPS are silicon wafers, covered with a 10 nm titanium adhesion layer and a 80 nm gold layer, to make them conductive and ground the thin film of material to characterize. This avoid the charging that could happen during photoemission processes. In the end, the substrates are cut to $7 \times 7 \text{ mm}^2$ squares. Then, the substrates, before use, are cleaned first in acetone, then in isopropanol and then an ulterior cleaning step is performed with oxygen plasma, all to avoid any contamination to the samples. Films are then spin coated on them, targeting thin films of around 100 nm (thickness is measured with a profilometer). Sides are then cleaned with a q-tip to avoid the films touching the sample-holder. All samples have been then conserved in nitrogen glovebox until they can be mounted. The mounting and grounding to the sample-holder is done carefully contacting the gold to the sample holder and thus to the ground. After being inserted in the load lock, the samples are left to degas until they can be inserted into the UHV (10^{-7} Pa) of the chamber, which usually is from 4 to 8 hours. This also removes most adsorbed particles. In fact, this is sufficient to suppress the O_2 traces, that is never present in the surveys performed on HgTe quantum dots films, even if the film preparation, ligands exchange and spin coating happen in air. In the HgTe survey contained in figure 2.1, the absence of oxygen is evident and evidenced.

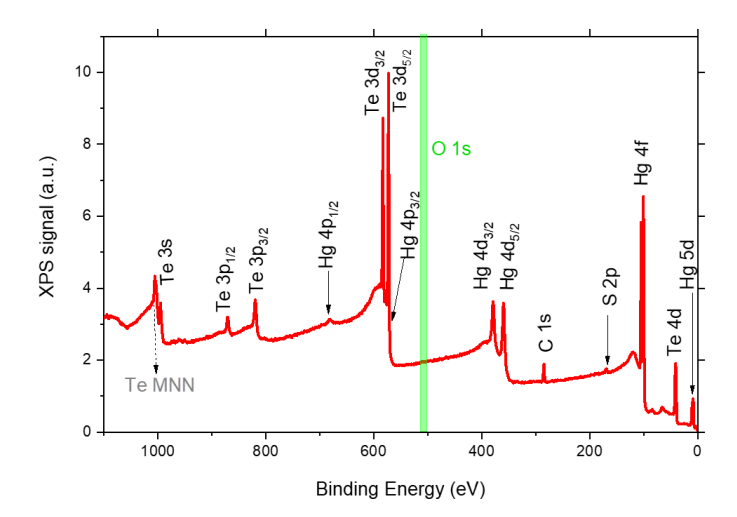


Figure 2.1: HgTe survey taken with Al source. Highlighted in green is the energy of the O 1 s core level (532 eV), that shows oxygen presence and is clearly absent

2.2 Photoemission set-up

The OCN group photoemission in-house set-up is a *PHI Genesis* XPS and HAXPES machine, with an additional UPS source. Sources are, respectively:

- XPS: Al K α , 1486.6 eV, monochromatic
- HAXPES: Cr K α , 51414.8 eV, monochromatic

• UPS He I, 21.2 eV+ additional He II, 40.8 eV, non monochromatic

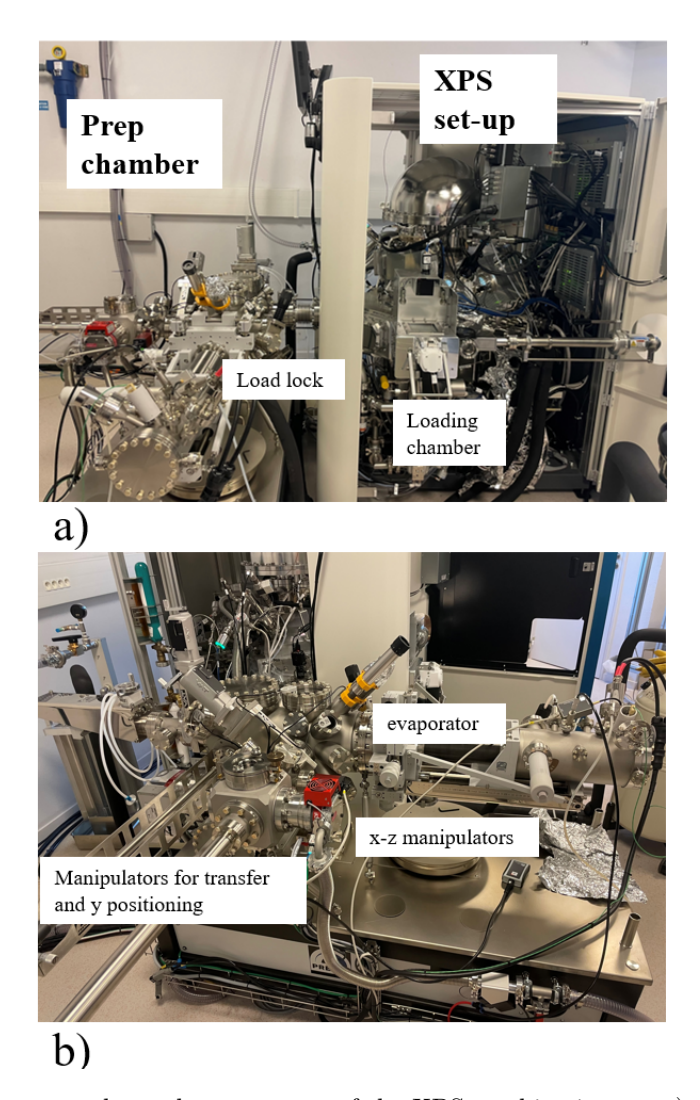
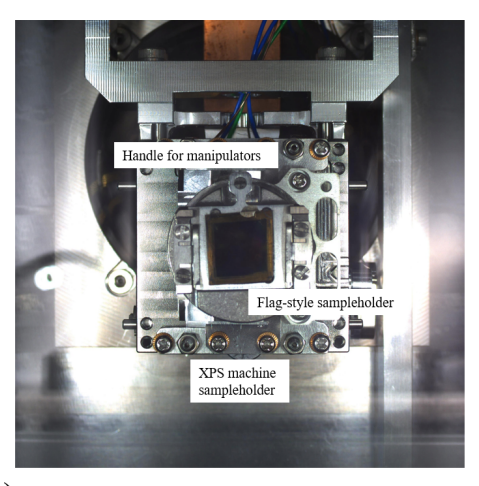
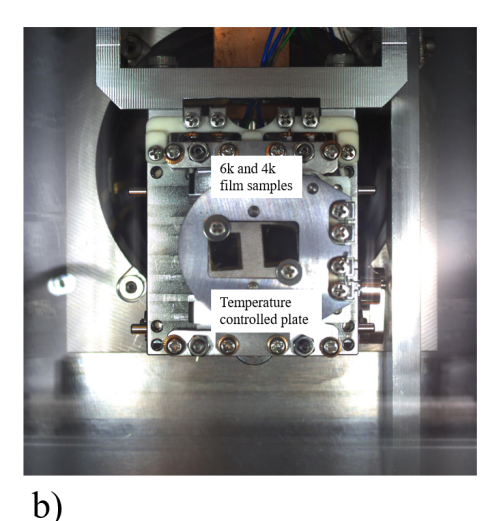


Figure 2.2: Different angles and components of the XPS machine in use. a) a front view of the XPS and preparation chamber,b) lateral view of the preparation chamber

Experiments described in this report are mainly taken with the Al source, because the film are rather thin and do no present any buried interface to analyze, so a surface analysis is appropriate. On the set-up, there is a variety of options that allows the study of materials in different conditions: in the contest of this thesis, the most important will be the preparation chamber and the control of the sample temperature.

Connected to the main XPS machine there is a *Prevac* Preparation Chamber, with the possibility of carrying out a variety of process, such as evaporation of different materials and high temperature baking, and then re- analyzing the sample in the main chamber.





a)

Figure 2.3: Detailed view of the samples and sample holders in the load lock chamber. Figure a) is the sample holder used for preparation chamber functionalization, with its detachable flag-style sample holder, compatible with the manipulators in the preparation chamber. b) is a sample holder with temperature control, localized on the plate area where the samples are held. The Ti screws used for mounting and grounding are visible

Analysis can be carried out at different temperatures, to analyze any modification happening in this case: one of the sample holders in use can be, during XPS measurements, heated until 500-600°C, and, more interestingly for the content of this report, cooled down to -100°C. The cooling process is obtained with the use of liquid nitrogen, that is circulated in a cooling line and cools directly the sample-holder. The system allows to set intermediate temperatures, maintained through a Proportional–integral–derivative (PID) controller. Temperature measurements are taken with a thermocouple integrated in the specific sample holder.

2.3 Photoemission measurements

The resolution and the scale of an XPS set-up depend strongly on the energy analyzer. In most cases, as is the case in our set-up, it is an hemispherical analyzer, consisting of two spheres, conductive and concentric, held at different, specific voltages. This makes it so that only electrons with a specific energy will go through the set-up and be detected. This energy is the Pass Energy, and more precisely, only electrons with energies comprised between $E_{pass} - \Delta E$ or $E_{pass} + \Delta E$. For a given set-up, the ratio between the two, $\frac{\Delta E}{E_{pass}}$, is fixed, so an high pass energy lowers the resolution and vice versa.[35][28].

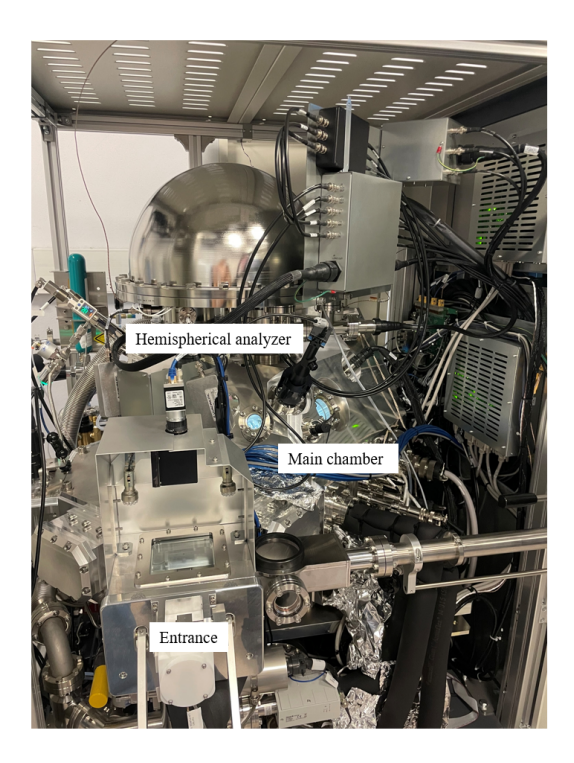


Figure 2.4: Detailed view of the XPS set-up, highlighting the analyzer

The pass energy do not have a direct relation with the original kinetic energies of the electrons; these are scanned with an energy step by the lens before the hemispherical analyzer, that slow them down so that the electrons of the desired \mathcal{E}_K arrive to the entrance with an energy equivalent to the pass energy. The Pass Energy is chosen by the operator conducting the XPS measurement. Another important concept is the context of sweeps, the number of times over which a spectrum measurements is repeated and averaged on. An high number of sweeps will improve the signal to noise ratio, but also increase the time.

A typical set of measurements on a sample consists of mainly 4 types of measurements, as presented before in chapter 1.

- a survey, to have an overview of the peaks presents, so on a big range. This spectrum is taken with an high Pass Energy, because there is not the necessity of particularly high resolution
- the different peaks, taken with lower pass energy, on a smaller range, centered on the core levels binding energy of interest. More precisely, three peaks are taken to characterize HgTe quantum dots, Te 4d, Te 3d, Hg 4f.
- a valence band measurement, so at low binding energies. A commendable choice could be taking the valence band and the very first core level that appears, because valence band is inherently less sharp.
- a cutoff, with an applied voltage

2.4 Data processing: peak fitting

A fundamental part of XPS measurement is then the peaks fit. This allows to recover the precise binding energy of the core level of them, and gather information on the photoemission peaks provenance.

All photoemission spectra will present an increasing background for any of the peaks, due to the inelastically scattered electrons that happens to have final kinetic energy in the range. Numerous choice of backgrounds can be made, but discussing all of them is out of the scope of this report. We will focus on the two used: Linear and Shirley.

The linear background is the simpler choice, but often can be very effective. It is only appropriate if the peaks background follow a straight line, but this is often the case if peaks analyzed are sufficiently narrow. Therefore, due to the choices made into peaks measurements, the use of linear background was often an appropriate choice. Shirley background is very useful in case a step is present[28], i.e. if the background before and after a peak appears mostly flat, but at different levels. In this case, the background is calculated relying on the assumption that the number of inelastically scattered electrons contributing to the back ground is directly proportional to the total photoelectron flux. Hence, the background intensity at the binding energy E_B is proportional to the total peak area in the energy range extending from the low binding energy side of the spectrum to E_B . The function used to calculate the Shirley background and other background alternatives are presented in the appendixes.

Peaks have are not infinitely sharp lines of emission, and their shape comprises of a Gaussian and a Lorentzian contribution. The Lorentzian comes from the lifetime of the emitted state, and is thus due to the nature of the electronic levels, the Gaussian relates to the broadening due to the uncertainties in the measurement, so the energy resolution, the broadening of the source energy, and other contribution of broadening (one that could be relevant in this thesis is the thermal vibrations contribution). Here they are

$$L(E_{Bp}) = \frac{1}{\pi} \cdot \frac{\frac{\text{FWHM}}{2}}{(E_{Bp} - E_{B0})^2 + (\frac{\text{FWHM}}{2})^2}$$
(2.1)

where E_{Bp} is the binding energy in each point, E_{B0} is the binding energy of the core level center, and FWHM is the full width at half maximum of the core level.

$$G(E_{Bp}) = \frac{1}{\sigma\sqrt{2\pi}} \cdot \exp\left(-\frac{(E_{Bp} - E_{B0})^2}{2\sigma^2}\right)$$
(2.2)

where σ is the standard deviation of the peak, (the full width at half maximum is related to σ by $FWHM = 2\sqrt{2 \ln 2} \cdot \sigma$). The most physically justified and appropriate choice for the representation would be a Voigt function, a convolution between the two.

$$V(E_{Bp}) = \int_{-\infty}^{\infty} G(E_{Bp'}) L(E_{Bp} - E_{Bp'}) dE_{Bp'}$$
(2.3)

However, this is not an analytic form, and thus is more complex to use. For the studies present in this report, a simpler weighted product of the Gaussian and Lorentzian functions was preferred, as implemented in the software used, CasaXPS. The function used is reported below:

$$GL(E_{Bp}, E_{B0}, F, m) = \frac{exp(-4ln2(1 - \frac{m}{100})\frac{(E_{Bp} - E_{B0})^2}{(FWHM)^2})}{1 + 4\frac{(E_{Bp} - E_{B0})^2}{(FWHM)^2}}$$
(2.4)

where m is the ratio of the contribution of the Lorentzian and gaussian. GL(100) is a pure Lorentzian and GL(0) a pure Gaussian.

Particular attention has to be made if we refer to fitting doublet peaks. In this case, the precise parameters presented in table 1.1 have to be respected, and peaks have to fitted with the same exact function. Both binding energy and spin orbit splitting value are often recoverable from the literature, and allows to obtain more information on the chemical shift and the type of bonds in the material by comparison.

An detailed example of the fitting of two of the most important peaks that are taken in the lab set-up is presented in figure 2.5; data refers to measurements on 6k HgTe quantum dots. Reported down there is also the precise binding energy and the distances obtained through data fitting in this specific case. The function is GL(60), the weighted product of Gaussian and Lorentzian as reported above, with 60 % Lorentzian contribution. This means that the contribution of the core level extension is still more important than all the other source of dispersion, and thus the measurement of the core level can be appropriately done. Background is chosen linear.

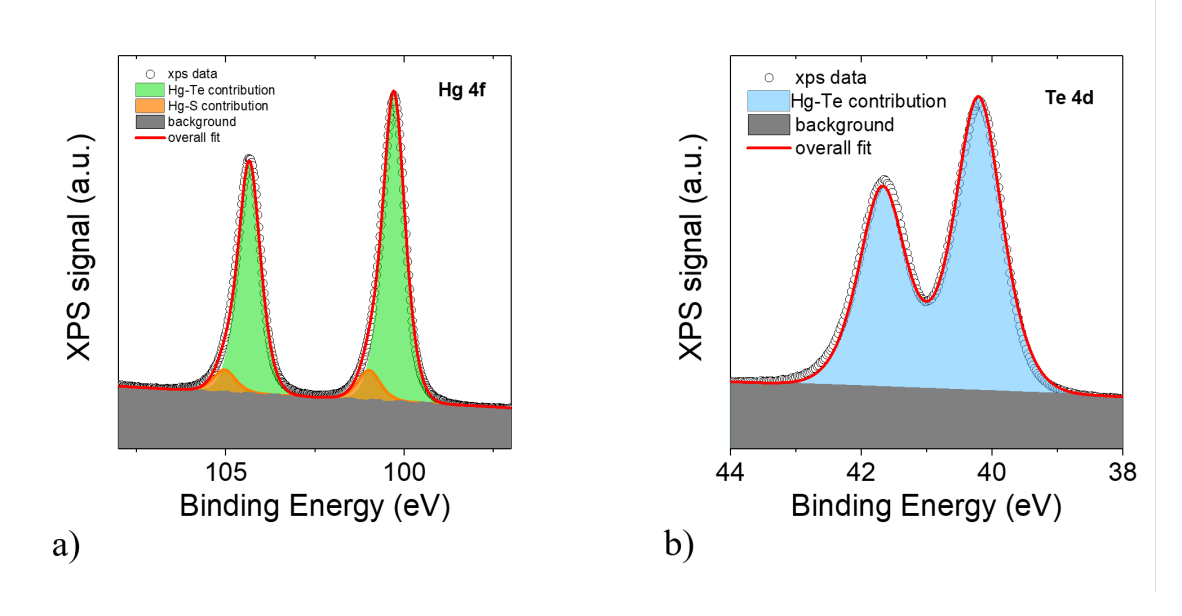


Figure 2.5: Fitted Peaks, starting set of data same as in figure 1.15. a) Hg 4f photoemission peaks, b) Te 4d photoemission peaks

	Hg-Te contribution (green)	Hg-S contribution(orange)
Spin orbit splitting distance (eV)	4.05	4.05
Binding Energy of Hg $4f_{\frac{7}{2}}$ (eV)	100.4	100.8
FWHM	0.77	0.77
Area ratio	0.75	0.75

Table 2.1: Fit of Hg4f

Table 2.2: Fit of Te 4d

	Hg-Te contribution (blue)
Spin orbit splitting distance (eV)	1.47
Binding Energy of Te $4d_{\frac{5}{2}}$ (eV)	40.3
FWHM	0.91
Area ratio	0.67

These show good accordance with expectation: area ratio of the peaks is respected. All the values reported are in accordance with the literature, for bulk materials and QDs[36][37][38][39]

Chapter 3

Alkali deposition for reduction of the work function

3.1 General context: Majority carriers, doping, and other electronic structure variation

Majority carriers are the dominant charge carriers, -electrons in n-type semiconductors or holes in p-type semiconductors- that contribute the most to electrical conduction. Their concentration can be deducted from the value in energy of the conduction and valence bands relative to the Fermi level: in n-type materials, the Fermi level is closer to the conduction band, resulting in a higher electron population, while in p-type materials, it is nearer to the valence band, resulting in a higher hole population. Bulk mercury telluride is generally p-type, but can be more or less dominated by holes depending on the growth process[40].

In HgTe QDs, however, the majority carrier type depends on shape and size, and subsequently band gap, of the QDs. In fact, the bulk band structure is characterized by a very different curvature of the highest occupied state with respect to the lower unoccupied states, leading to different effective masses. These differences result in a different behavior of conduction and valence band for varying sizes[41]. Smaller QDs and more confined HgTe structures such as nanoplatelets, that feature larger band gaps, have a p-type behaviour, confirmed also by the behaviour of NPL based transistors [41]. As the size increase, the conduction band approaches the Fermi level more rapidly than the valence band, determining first an ambipolar and then an n-type behaviour. For band gap below around 250 meV, the conduction band is below the Fermi level, determining degenerate doping, i. e., strong presence of one type of carriers without the addition of any impurities [42]. This condition is often referred as self doping and is present in other quantum dots, e. g., Ag₂Se[43], and PbS[44]. In this particular section, all the result we discuss are on quantum dots with absorption edge at 6000 cm^{-1} (termed as 6k), which has an ambipolar behaviour. In the next section, other QDs with absorption edge at 4000 cm^{-1} and $3000 \ cm^{-1}$ will also be used, which show, respectively an ambipolar behavior and a more electron dominated conduction (figure 3.1).

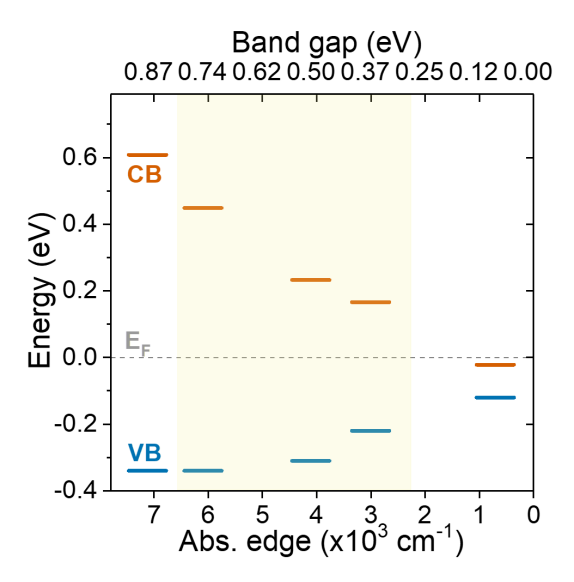


Figure 3.1: Band diagram for different QDs sizes. The QDs used in this report are highlighted in yellow. Adapted from [41].

Typical doping with impurities, as done in bulk semiconductors, is rather complex and immature in QDs. Some results have been obtained with Ag [45] and Cu [46], but these creates only new trap states, and do not generate any free charges as in traditionally intended doping. Nonetheless, alternative options for tuning QDs electronic structure are being explored.

A particular interest resides in engineering a lower work function of the material. A lower work function is desirable as it facilitates electron emission and influences interfacial charge redistribution in heterostructures. In fact, the difference in work function between materials drives charge redistribution at their interface, leading to different bending of the bands at the interface, and this effect is crucial for the functioning of electronic devices. An obvious example would be the pn junction, where however the work function is varied by doping. Engineering the work function without doping still allows for example to improve or avoid the injection of carriers in a material through band bending at the interfaces of the junction.

One of the most important method to lower the work function of a material involves the creation of a surface dipole. The dipole involved has its positive side pointing toward the vacuum, which lowers the energy barrier that electrons need to overcome to escape the material. The presence of this dipole changes the work function, in the following way.

$$W_F = W_{F,initial} - \frac{e\mu_s}{\epsilon_0 \epsilon_r} \tag{3.1}$$

where e is the electron elementary charge, ϵ_0 is the vacuum dielectric constant, ϵ_r , is the relative dielectric constant of the material functionalized, μ_s is the magnitude of the dipole per surface unit.

This dipole can be created with various methods. Successes were achieved through ligand exchange [47]: different ligands will create different dipoles on the QDs surfaces and thus tune the response. It is however a method that is not necessarily best suited for all electrical use: too long ligands would hinder the charge transport between adjacent quantum dots.

3.1.1 Previous results from Potassium deposition

A previous study conducted in the group [39] had already explored the possibility of tuning the work function with alkali deposition.

Alkali metals, when adsorbed on a surface, lower the work function of a wide range of materials through the formation of a surface dipole. This effect arises from their chemical nature: as group I elements in the periodic table, alkali metals have a single valence electron, which can easily interact with the substrate and induce a charge redistribution at the interface. This behavior has been well documented in metals [48] as well as in typical semiconductors such as silicon [49]. The adsorbed alkali stays at the very surface, and the dipole is formed in different ways depending on the material: it either creates a partial charge transfer, due to the bonds between the starting materials and the adsorbed atoms (in a majority of metals) or creates a polarization that resides in its valence band (attested on W and on some semiconductors)[50].

This earlier study was performed on HgTe 6k and 4k samples, and the alkali of choice is Potassium. All experiments were performed at TEMPO beamline of SOLEIL synchrotron facility. Potassium deposition was performed, and its trace was evident after some depositions, in the XPS survey in fig 3.2 a) and b). Moreover, it was evident that the HgTe core levels had no change in their overall appearance and in their binding energy. This confirmed that the potassium did not cause any charge transfer. The only significant change observed in XPS data was the work function variation of the HgTe films with K (fig: 3.3).

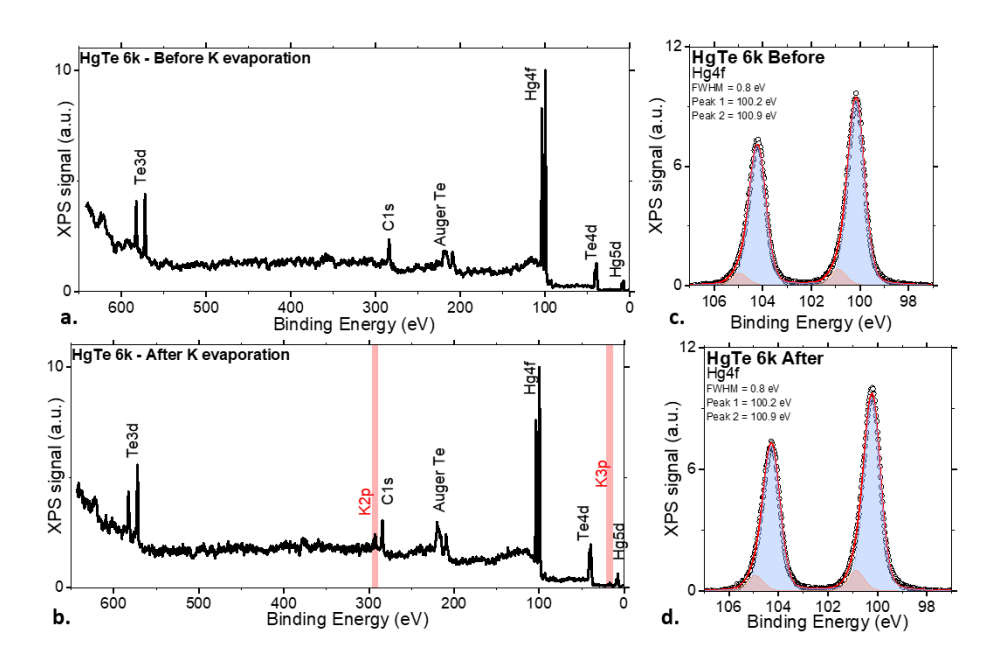


Figure 3.2: Surveys and Hg 4f core levels , presented in article [39], before and after potassium deposition

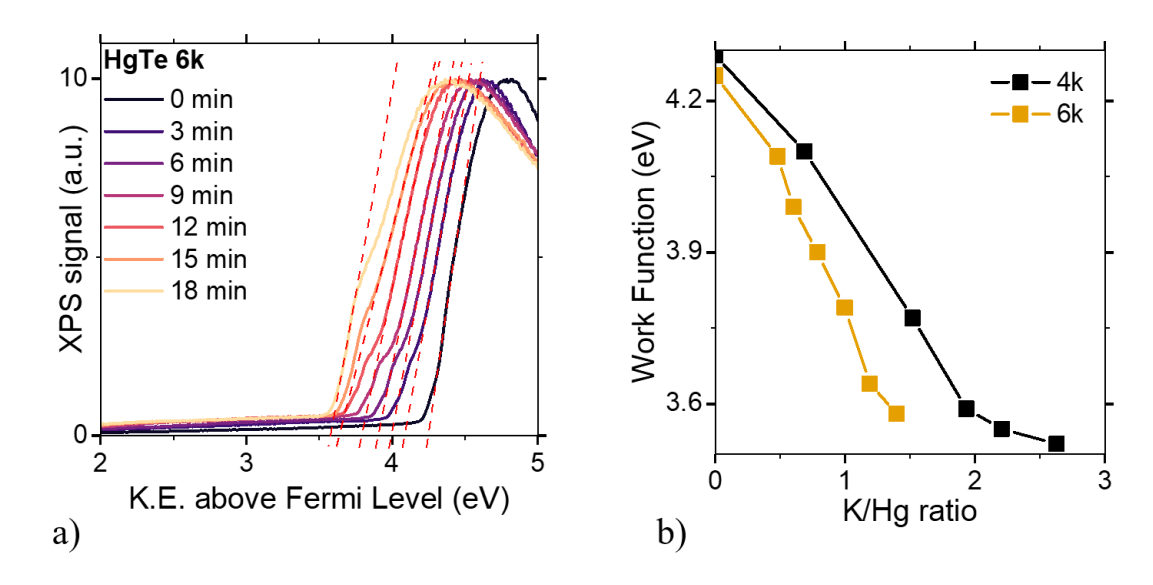


Figure 3.3: Cut offs taken on 6k samples at different deposition times, and plot of the work function in function of the amount of potassium

The work function in fact decrease steadily with the increase of Potassium coverage. Subsequent addition of potassium configures as an ulterior lowering of the work function. Some slight differences are evidenced with the two sizes of quantum dots, that suggest that the interface of them play a role, but the overall trend is consistent between the two cases.

3.2 Measurements and results

To expand on these previous results, it was deemed interesting to confirm the tendency for other alkali, and to investigate the eventual differences.

My experiment consisted thus ib a study of the effect of Cesium deposition on a HgTe 6k film. Cesium, Cs, is an alkali metal, with atomic number 55, relevantly heavier than potassium (atomic number= 19). It is relatively easy to deposit in an evaporator, because it evaporates at a lower temperature than most other metals, which makes it a great candidate for this experiment.

On metals, it is attested that the work function shift is more pronounced with heavier alkali, with the same quantity of adatoms adsorbed into the surface [51]. It was thus expected that the shift would be evident from the start, as in potassium.

Due to the fact that a similar trend was evidenced in the behaviour of the 6k sample vs the 4k sample, this experiment was performed only on one particular QDs size: 6k.



Figure 3.4: Photo of the deposition process in the preparation chamber, with a sample mounted on a flag stile sample holder, and the heated getter

The experiment was performed on the PHI Genesis lab set-up, using the evaporator integrated in the preparation chamber connected. An image of the process is shown in figure 3.4). The Cs source mounted is a Cs getter from SAES Getters. Before use, a 2.1A current was applied to the getter for one night, to degas any adsorbed contaminants, such as water, that could have been absorbed during the in-air mounting of the getter. Deposition is performed by applying a 5.1A current to the getter; this current is just above the expected emission treshold value of 4.7A, to have a slow and controlled deposition. To have a reference, and ensure that a similar quantity of alkali is deposited each time, all depositions were timed. Deposition timing starts when the target current is reached, and the sample is exposed directly to the getter.

This deposition happens at room temperature, as in the previous experiment with potassium. It is then expected that the alkali will be highly mobile, and deposit throughout the surface in a submonolayer regime. This will be confirmed by all the experimental data, from which the Cs coverage and impact can be extracted. From the surveys (in figure 3.5, the presence of Cs was very evident already at the first deposition, after three-minutes. The cross section of Cs 3d when irradiated with Al source is rather high, and so the peaks are especially evident. After the second deposition,- after a total of 6 minutes- a strong increase of the Cs 3d core level was observed, confirming the effectiveness of the progressive deposition process.

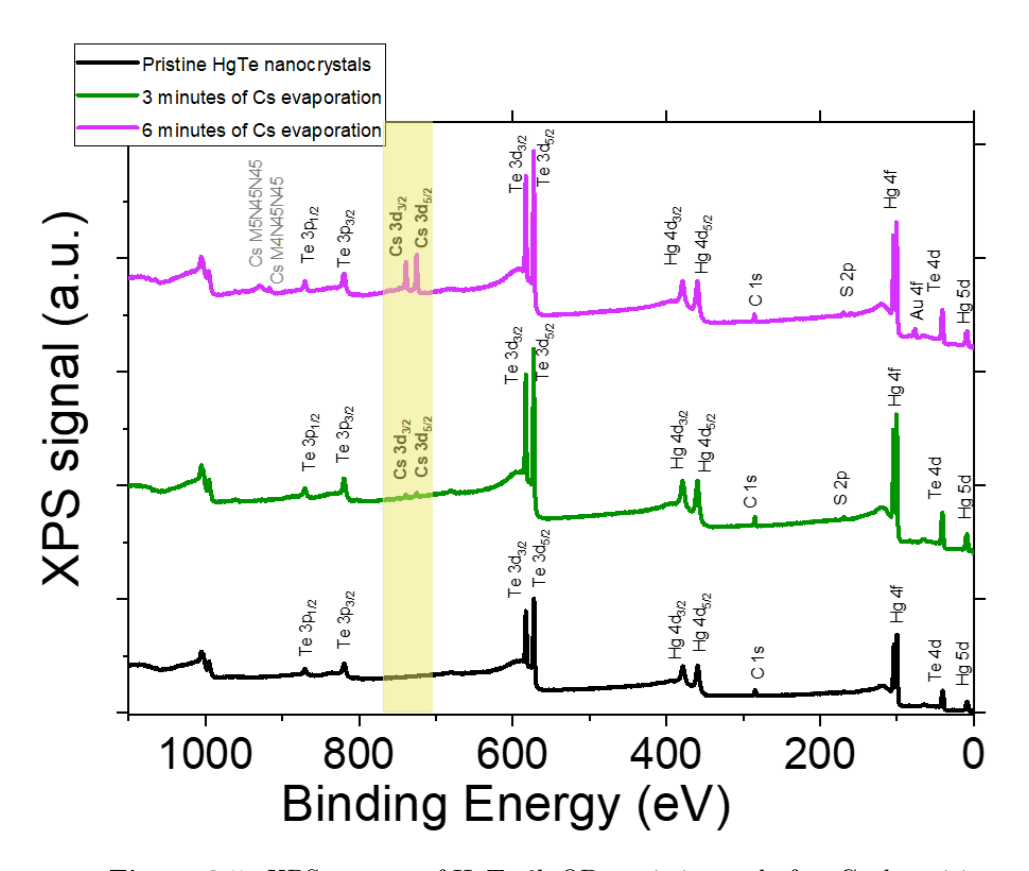


Figure 3.5: XPS surveys of HgTe 6k QDs, pristine and after Cs depositions

To have a better indication of the Cs depositions, XPS measurements were then taken specifically on the Cs 3d core levels, and these are then fitted; see figure 3.6.

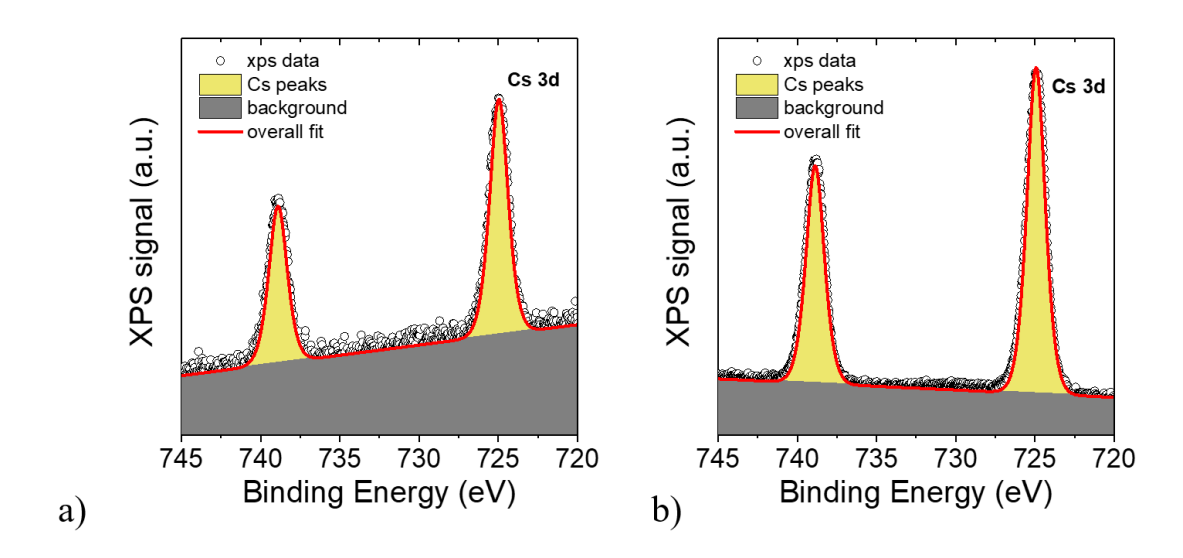


Figure 3.6: Cs 3d core levels: a) after 3 minutes of Cs deposition and b) after 6 minutes Cs deposition

Peaks are fitted with a multiplication of Gaussian and Lorentzian, with 55% of Lorentzian contribution, and a linear background was subtracted. The parameters obtained are the same for both core levels, confirming that no chemical shift is happening. (Table 3.1 shows the fitting parameters for the Cs 3d core levels.)

Table 3.1: Fitting parameter for Cs 3d

$E_B ext{ of } 3d_{5/2}(eV)$	724.9
SO Distance (eV)	14
FWHM (eV)	1.4

Binding Energy and spin orbit splitting are in accordance with the NIST Database for Cs, and precisely with what is contained in the following article. [52] .

Core levels and Valence band

Comparison of the following core levels is then performed: Hg 4f, Te 4d, Te 3d.

On them, Cs deposition cause minimal changes. No shift is happening, no overall trend can be evidenced. No variation in the core level binding energy is observed. To confirm this, and to explore the reason of the variation evidenced on the high binding energy side of the Hg 4f peaks, these core levels are fitted.

Fit are performed with GL(70) for Hg 4f and GL(55) for the broader Te 4d. Data from the fit are reported below.

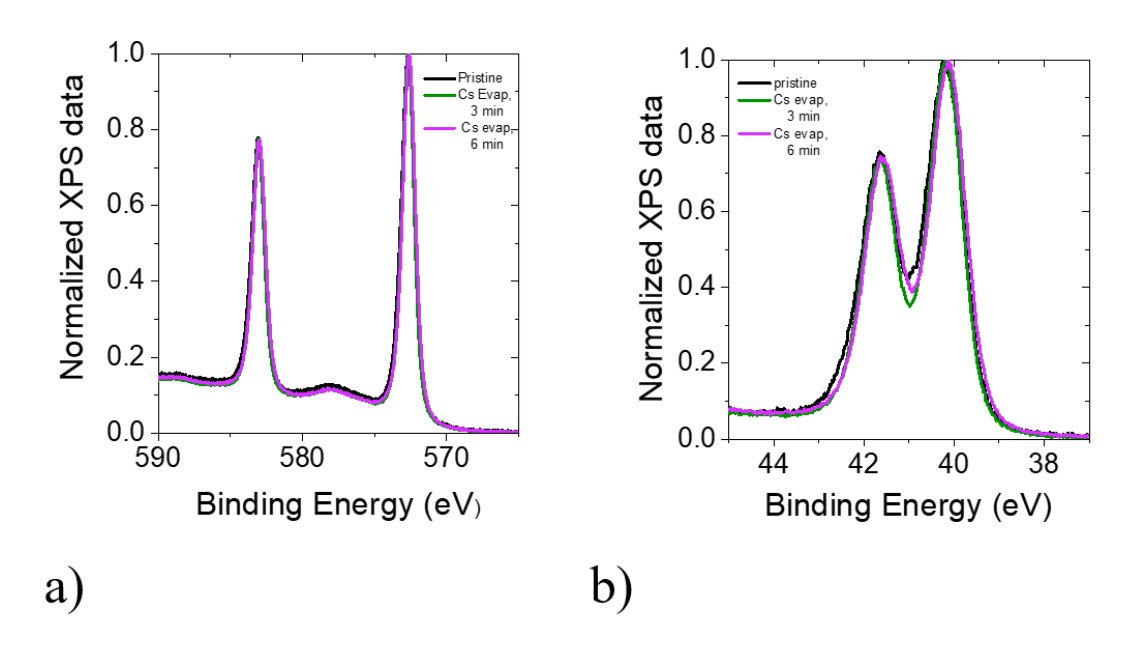


Figure 3.7: Comparison of the Te 3d and Te 4d core levels before and after Cs depositions

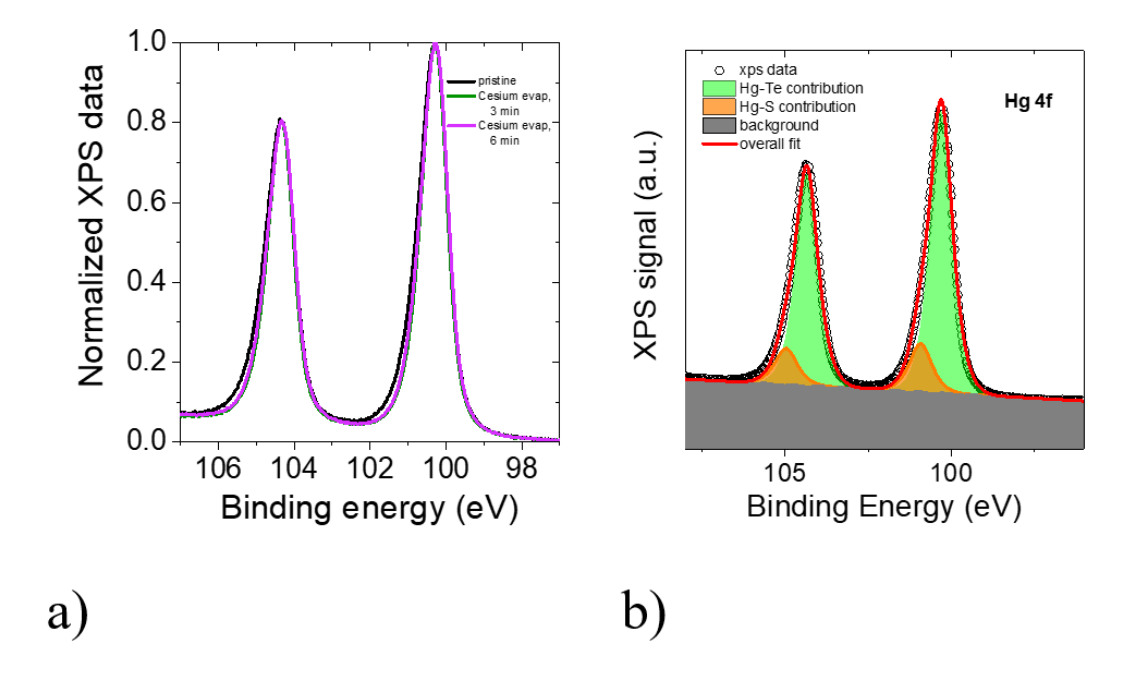


Figure 3.8: Comparison of the Hg 4f core level before and after Cs depositions, and fit highlighting the two contributions of the spectrum (Hg-S contribution is progressively diminishing with the depositions)

Table 3.2: Fit of Hg4f on pristine sample

	Hg-Te contribution (green)	Hg-S contribution(orange)
Spin orbit splitting distance (eV)	4.05	4.05
\mathbf{E}_B of Hg $4f_{\frac{7}{2}}$	100.3	100.9
FWHM	0.78	0.78
Ratio of the two contributions	$\frac{Hg-S}{Hg-Te} = 0.17$	

Table 3.3: Fit of Hg4f after 3 minutes of Cs deposition

	Hg-Te contribution (green)	Hg-S contribution(orange)
Spin orbit splitting distance (eV)	4.05	4.05
E_B of Hg $4f_{\frac{7}{2}}$ (eV)	100.3	100.9
FWHM (eV)	0.73	0.73
Ratio of the two contributions	$\frac{Hg-S}{Hg-Te} = 0.12$	

Table 3.4: Fit of Hg4f after 6 minutes of Cs deposition

	Hg-Te contribution (green)	Hg-S contribution(orange)
Spin orbit splitting distance (eV)	4.05	4.05
E_B of Hg $4f_{\frac{7}{2}}$ (eV)	100.3	100.9
FWHM (eV)	0.74 0.74	
Ratio of the two contributions	$\frac{Hg-S}{Hg-Te} = 0.14$	

It is fact evident, from 3.8 and from the ratios presented in the tables, that in Hg 4f the contribution due to the compound between Mercury and Sulfur, from the ligands, is slowly decreasing with the deposition process. The deposition chamber is rather small, so some of the heat of the getter could be reaching the sample. Due to this involuntary heating, some ligands could be degrading.

Table 3.5: Fit of Te 4d on pristine sample

	Hg-Te contribution (blue)
Spin orbit splitting distance (eV)	1.47
Position of Te $4d_{\frac{5}{2}}$ (eV)	40.2
FWHM (eV)	0.95

Table 3.6: Fit of Te 4d after 3 minutes of Cs deposition

	Hg-Te contribution (blue)
Spin orbit splitting distance (eV)	1.47
E_B of Te $4d_{\frac{5}{2}}$ (eV)	40.2
FWHM (eV)	0.88

Table 3.7: Fit of Te 4d after 6 minutes of Cs deposition

	Hg-Te contribution (blue)
Spin orbit splitting distance (eV)	1.47
\mathbf{E}_B of Te $4d_{\frac{5}{2}}(\mathrm{eV})$	40.2
FWHM (eV)	0.88

In the end the core levels maintain evidently the same E_B , and undergo no modification that suggest any change in their energy level, thus no charge transfer is reported.

The core levels fitting allows also to obtain an estimation of the covering of the surface in Cs atoms. There is in fact a correlation between the ratio of the areas of the fitted core level, and the stoichometric ratio of the components. In the potassium deposition case, this comparison is particularly easy due to the presence of the Hg 5d core level quite close to a K peak, K 3p. Having them in close proximity allows to compare them directly, as they also present similar cross sections. In this specific case, the ratio between the areas of the potassium peaks over the Hg peaks can be taken as the ratio of the 2 quantities, and thus, as a surface coverage indication. In the Cs case, the most evident core levels for the alkali are rather far from any relevant one of Te or Hg. In this other case, it is necessary to correct the ratio with R.S.F, the relative sensitivity factor, a parameter that takes into consideration the difference in cross section and transmission to the analyzer of the different core level, in the following way:

$$\frac{\frac{A_j}{RSF_j}}{\frac{A_i}{RSF_i}} \tag{3.2}$$

Different calculations are available for RSF values. In this work the values contained in Scofield library are used [53]. The deposition of Cs is thus discovered to not have a linear trend with respect to the Cs/Hg ratio: we obtain in fact a Cs/Hg=0.020 after the first deposition and a almost ten-times larger value after the second, with Cs/Hg=0.18. This suggest that the deposition yield of the getter, and the sticking of the Cs, increase over time.

Similar ratios are obtained also comparing the area corrected with the RSF of the Te 4d peaks, which confirm the general correctness of this estimation; mercury and tellurium are present in a 1:1 proportion, and thus should have an identical ratio with Cs. So, after 6 minutes, a coverage of about 20% of Cs was reached on the surface of the film.

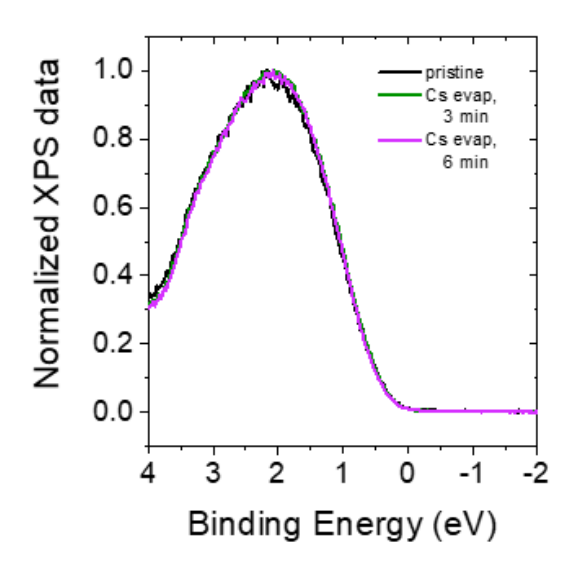


Figure 3.9: Comparison of the top of the valence band before and after the 2 Cs deposition

The behavior of the valence band is identical to the one of the core levels, is actually even more evident that no variation in its photo-emission spectrum is observed. The absence of change in the valence band confirms that the Cs is not releasing its free electron to act as a dopant, and thus there is no charge donation, even with the relative facility for alkali to become cations. All these results are in clear agreement with previous observations using potassium: no shift in the core levels or the valence band was detected, no evidence of additional free carriers introduced by the alkali, and thus no indication of doping effects.

Work function

As expected, the main effect observed is on the work function. The first starting value, the work function of these pristine HgTe quantum dots, was 4.3 eV, which is in line with the range documented, between 4.2 eV,[39], and 4.5-4.6 eV[10].

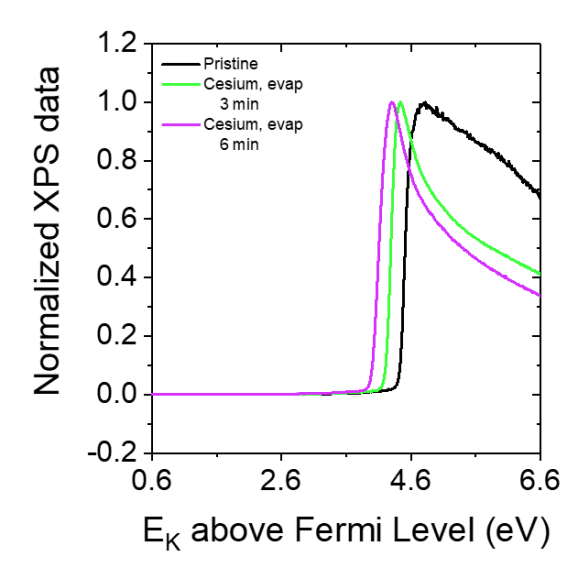


Figure 3.10: Comparison of the cut off before and after the two Cesium depositions

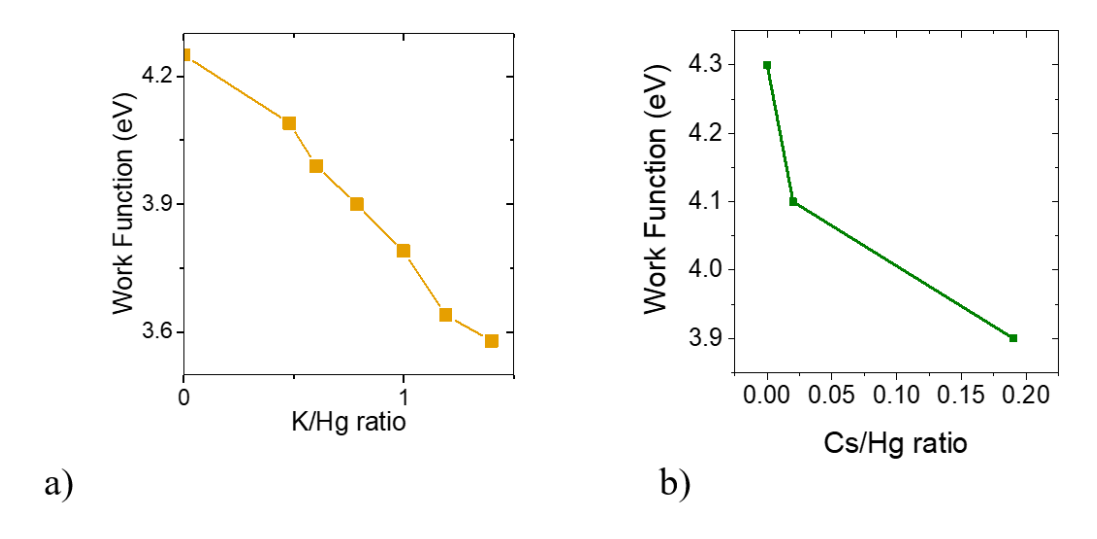


Figure 3.11: a) Plot of all the work function value with respect to K/Hg, adapted from [39] and b) Plot of all the work function value with respect to Cs/Hg

After the first deposition, the shift to lower kinetic energy of the cut off, and thus the diminution of the value of the work function, was indeed evident. In fact, the new work function value was 4.1 eV. After the second deposition, the behaviour was also very similar, with another variation of 0.2 eV, bringing the work function value down to 3.9 eV. The general trend of work function diminution thanks to alkali presence is thus confirmed. The distance of the Fermi Level and the vacuum level is relevantly reduced. This confirms that the presence of alkali reduces the work function significantly, even at relatively low coverage, 2% and 20% of the surface.

This variation can be attributed without any doubt to the alkali, without any other first order

contribution. The gold presence that is registered in the survey after the deposition, probably due to involuntary heating during deposition, is not influencing the work function measurement. The presence of the metal photoemission peak is very low and its work function is between 5.3 and $5.5~{\rm eV}[54]$, relevantly higher than pristine HgTe, while the shift observed in our case was towards lower values.

These findings match what was observed in potassium (see figure 3.11). The same overall trend is found for both Potassium and Cs, with a shift correlated to the alkali presence and continuing with further evaporation. The effects on the work function, for similar ratio of alkali, are of the same order of magnitude. Cs seems to have a stronger effect on the work function than potassium, in fact we observe a diminution of 0.4 eV with 20% of Cs/Hg, while the same variation is reached at circa K/Hg=1. Although exact ratios are difficult to quantify, this variation is coherent with what was expected. This trend is consistent with observations in both metals [51] and semiconductors, where heavier alkali metals tend to induce a more pronounced reduction in the work function.

In both K and Cs deposition cases, the value of the reduced work function is still rather far from the one of the adsorbed alkali, which are respectively of 2.1 eV and 2.3 eV [55]. This, together with the low surface coverage, confirms that the observed reduction in work function arises from the formation of a surface dipole, rather than from the work function of the alkali metal itself appearing in the XPS data.

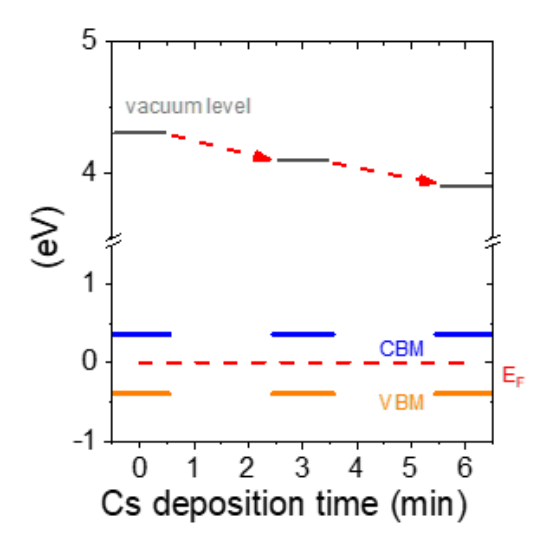


Figure 3.12: Band diagrams in function of deposition time.

In the end, a good accordance of results was found, which suggest that alkali deposition is an effective way to lower HgTe work function, and multiple alkali options can be exploited. It is also confirmed that this effect occurs without generating more free carriers, and the dipole formation is the main driving mechanism. Tuning the work function through alkali deposition seems, in conclusion, to be an effective option.

However, both K and Cs are rather heavy and large alkali. There surely is an interest in repeating these measurements with lighter alkali such as Li, which are reported to cause less work-function

reduction, to better understand if this behaviour is somewhat affected by the shape of the interfaces or by some specificity of the alkali in questions. A smaller atom could even intercalate between the QDs in the film and act more as a traditionally intended dopant.

Chapter 4

Photoemission study of HgTe at low temperature

4.1 General contest

4.1.1 Photodetectors: Dark current and lowering temperature

HgTe film's conductance can be modulated by the light response. The current of these film under appropriate illumination is given by two contributions:

$$J_{tot} = J_{dark} + J_{opt} (4.1)$$

Where J_{opt} is the component created by photogenerated carriers, and J_{dark} is the component always present, independently from illumination, and is due to all the other phenomena generating free carriers. One of the most relevant source of this is thermally activated carriers, carriers freed by thermal agitations. This latter component becomes especially significant in IR detectors: the thermal energy K_BT is 26 meV at 25°C, which is comparable to the transition energies of the photogenerated carriers, which are rather low in the infrared range.

As such, many short-wave infrared (SWIR) and most mid-wave infrared (MWIR) detectors are operated at low temperatures to suppress dark current. However, a lower temperature could impact the electronic structure of a material. In fact the band gap dependence on temperature is a well known effect in semiconductors[56].

On HgTe QDs side, prior experimental work had already confirmed that there is a change in the optical absorption of differently sized cQDs [57]. However, absorption only confirms the band gap extension, but no information on the energy difference of the valence and the conduction band with respect to the Fermi Level can be extracted from them. This brings an important gap of information: the energy distance of the VB and CB with respect to the Fermi level determine the p-type, n-type or ambipolar behaviour of the material, and knowing their precise energy value is also fundamental to properly match, for example, materials that maximize electron and hole extraction in a photodiode.

Photoemission measurements offer the possibility of probing the top of the valence band, the work function of the materials and the electronic core level, that are a direct indication of the position of the filled electronic states. So there is an interest in performing XPS measurements at low temperature on differently sized HgTe nanocrystal.

4.1.2 Band gap trend in temperature in HgTe Quantum Dots

More precisely, Moghaddam et al.[57] performed a comprehensive study of confined HgTe structures, of different sizes, shapes (quantum dots and nanoplatelets) and thus quantum confinement and band gap. They report the non linear trend for the band gap variation in temperature shown below. Larger QDs (with smaller band gap) exhibit a red-shift, and thus a band gap reduction, shown in figure 4.1 a), which progressively become less pronounced for smaller ones. More confined structure would even present no band gap modification, as in figure 4.1 b), and even band gap enlargement in the Nanoplatelets case. The total trend is shown in figure c) 4.1.

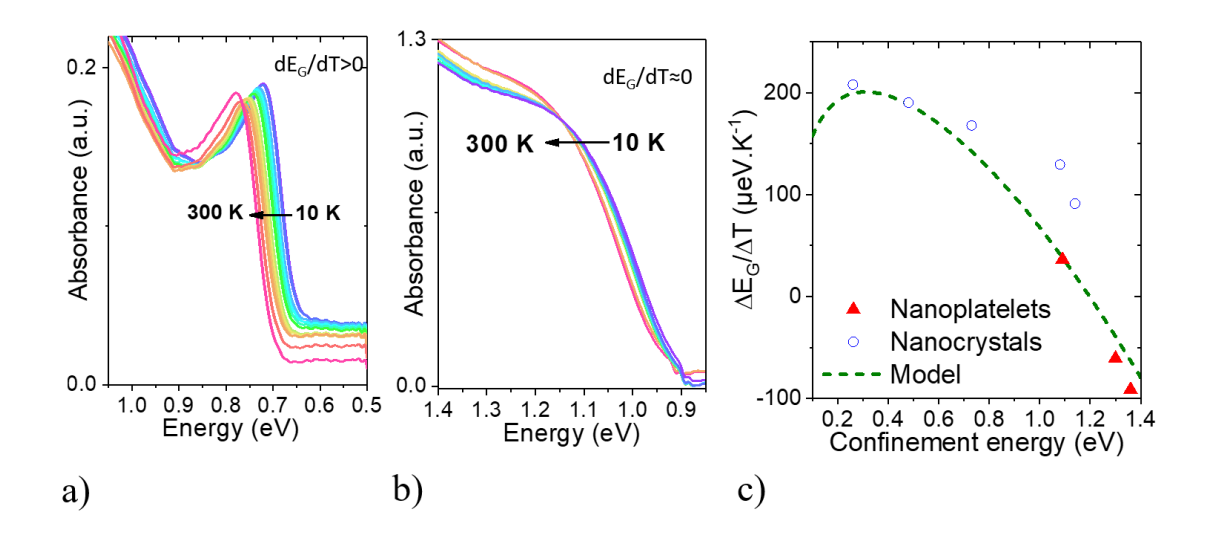


Figure 4.1: Variation of the band gap of different QDs in temperature; a) absorption measurements of large size QDs, showing a red shift as the temperature is lowered, b) absorption measurements of small size QDs, showing no shift and c) Band gap variation in temperature for different confinement energies, experimental data and proposed fit. All adapted from reference [57]

A naive explanation based on thermal contraction of the QDs, does not align with these experimental observations. Thermal contraction would determine, in a first approximation, an enlargement of the band gap (which should go approximately as $\frac{1}{R^2}$, or, more specifically, in HgTe $\frac{1}{R}$) not a diminution. Moreover, the opposing trends observed across different QD sizes contradict this explanation, suggesting that thermal contraction effects are negligible.

Instead, the dominant mechanism is attributed to the changes that the band structure of bulk HgTe undergo at lower temperatures; These changes in the bulk band structure, as seen in chapter one, influence the quantized states of the [58].

In similar compounds such as cadmium chalcogenides, it is common to observe a blue shift of the absorption as the temperature is lowered. However, mercury telluride display an inverse behaviour, so, with a band gap that reduces as temperature is lowered, like in traditional semiconductors such as silicon. This effect stems from changes in Γ_8 , the band that acts as the conduction band. HgTe dispersion is, as anticipated in chapter 1, not parabolic, and the effective mass approximation holds only for 1% of the k values. The shape of the area that we are mostly concerned of, between Γ and X points, is approximately linear for a good part, and then it curves downward close to the

X point. $k \cdot p$ calculations, the semi empirical method that allows to reconstruct effective mass and band structure, shown in figure 4.2, evidence how this behavior evolves with temperature. The linear part of the bands, closer to Γ and k=0, is lowering with lower T while the curved area is increasing. This explains the lowering of the band gap extension in the bulk, and also on the QDs that are the object of our study, and the increase instead evidenced in NPL.

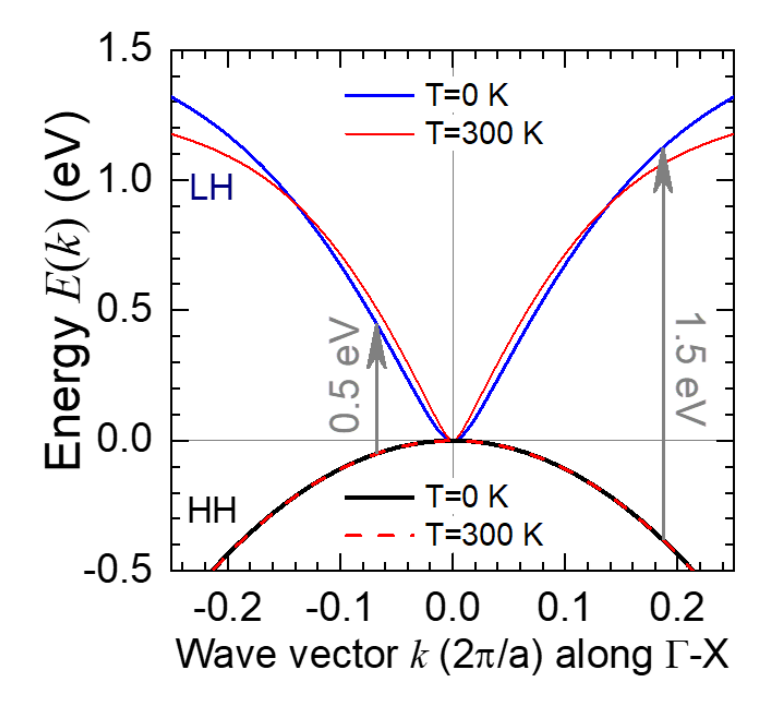


Figure 4.2: Effect of temperature on the Band dispersion, as calculated in [57]

4.2 Measurements and data processing

A set of measurements, as described in chapter 2, is taken at room temperature, at -100°C and at intermediate temperatures, on HgTe nanocrystal of 3 different sizes and thus band gaps, with absorption edges at 6000 cm^{-1} , 4000 cm^{-1} , 3000 cm^{-1} . The temperatures, more precisely, are 23°C, -25°C, -50°C and -75°C and -100°C. Cooling is performed with the use of liquid nitrogen, circulated in the apposit cooling line present in the sample holder. Measurements were performed following this timeline:

- Initial room temperature measurement
- Cooling to -100°C and stabilization of the temperature.
- progressive heating to intermediate temperatures and stabilization (from -100°C to -75°C, from -75°C to -50°C).
- Data acquisition for each set takes around 3 hours. During this time, the liquid nitrogen is consumed, and refilling the dewar while in use could damage the instrumentation, so no more than 2 or 3 set could be performed each day.

- cooling of the system to the lowest temperature still required and progressive heating from this.
- Final room temperature measurements, to ensure the reversibility of the process

A clean Au-on-Si substrate served as a control to monitor for potential instrumental shifts at low temperature. It provided a reference for the Fermi level calibration at each temperature.

4.2.1 Samples' characterization and intermediate data processing

6k sample

Initial surveys on the room temperature sample (fig 4.3 shows that there is no contamination from the substrate, so neither gold nor silicon are present, and no oxidation of the film, in fact there is no oxygen peaks. Only elements present either in the QDs, in their ligands (es sulfur) or in the exchange solution are localized.

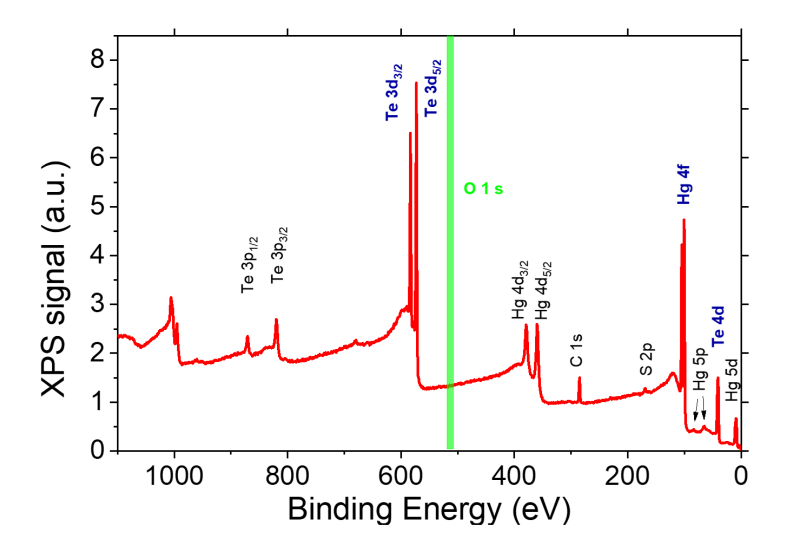


Figure 4.3: Initial survey, taken on room temperature 6k sample

Then the 3 core levels are taken and analyzed. A first comparison is performed: these core levels were normalized for comparative analysis. As it is evident from figure 4.4, there is a pretty clear trend: as the temperature is lowered, the peaks move to lower binding energies. This shift is uniform across core levels, suggesting a rigid band structure translation. No other relevant change is evidenced; no significant variations of the peaks appearances, of their area ratio, and of the spin orbit splitting is observed. Only second order phenomenon happening is a small reduction of FWHM of Te 4d, that is perfectly to be expected with the lowering of the temperature.

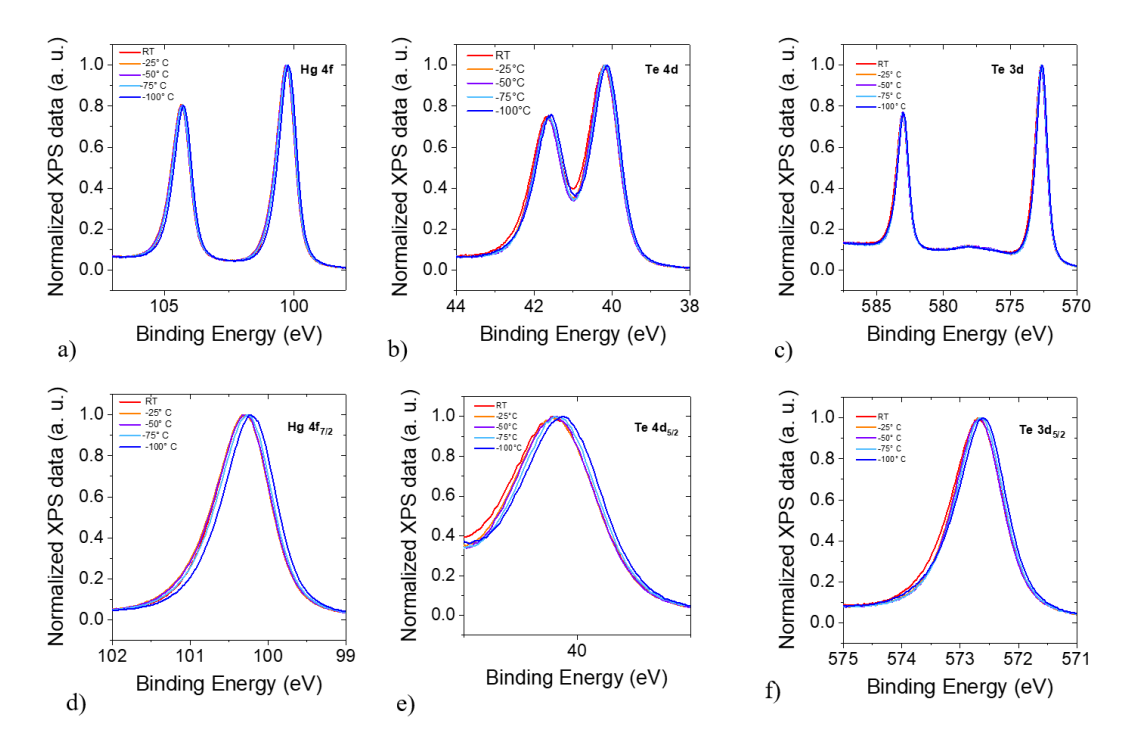


Figure 4.4: Variation of the 6k core levels with temperatures: a), b), and c) are the full Hg 4f, Te 4d and Te 3d doublets, and d)e)f) are a zoom of their lower B. E. feature

This rigid shift appears at a first glance to be correlated pretty well with temperature, lower temperatures cause a more relevant shift.

To confirm quantitatively this effect, shift needs to be measured. The most straightforward option seem to be fitting the core levels, recovering their energy and then comparing then. However, this introduces more error. The error in identifying a peak Binding Energy in this report is 0.01 eV. Due to the fact that each peak position is calculated and then subtracted, this initial error needs to be at least doubled, bringing to a 0.02 eV of error which will prove to be rather relevant in this contest. So, Hg 4f and Te 3d shifts are measured simply by offsetting them peaks taken at lower temperature of the quantity necessary to make them superimposable to those taken at room temperature. This process can appear, at first glance, rather simplistic, but in reality leads to the best results in term of error introduced at the data processing. It allow to see variations of the order of 0.005 eV, in fact, and it is not affected by the error propagation of the subtraction that other would have.

However, an exception had to be made for the Te 4d core levels, because of the reduction of the FWHM is at lower temperatures (figure 4.5). This process happens because thermal agitation is a great contribution to the gaussian dispersion of the core level. In this case, it is particularly evident due to the limited extension of the peaks. This made impossible for Te 4d to be measured in an appropriate way with the offset method, and made the fitting necessary. All Te 4d peaks are fitted with the same function shape, and same background. The function used in the fit is a Gaussian-Lorentzian multiplication where the percentage weight of the Lorentzian contribution is 60% (see chapter 2), and the background is always chosen linear.

In the end, the variation observed in each core level is around 80-90 meV at -100°C, and is

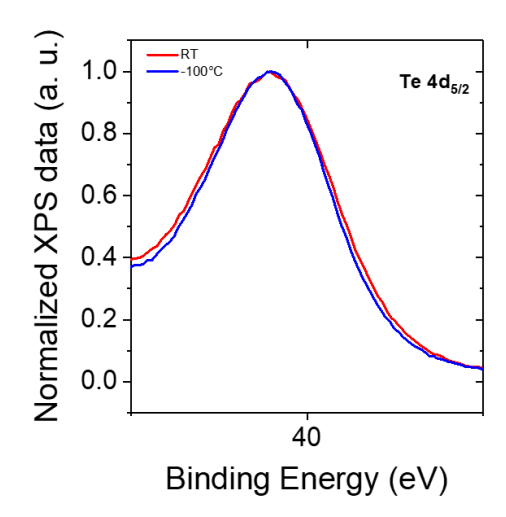


Figure 4.5: Superimposition of Te 4d peaks at room temperature and -100°C (shifted), that allows to see the variation in FWHM with T.

progressive, but not linear. An increase seem to onset around -75°C.

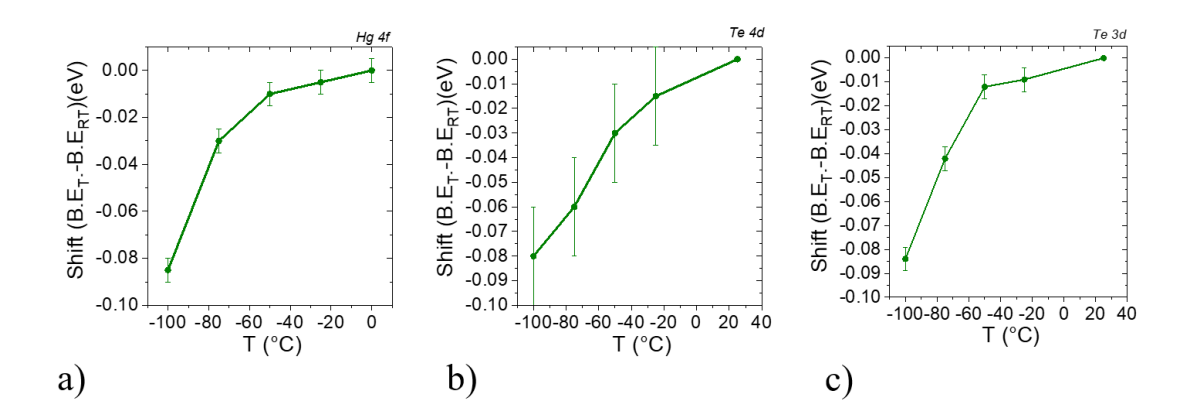


Figure 4.6: Shift of 6k peaks with respect to the temperature: a) Hg 4f, b) Te 4d, c) Te 3d

The valence band measurement is also taken, with a large range, to include also the first core level visible, which is the doublet Hg 5d. This choice allows to have an emission feature that has an easier treatment than the proper VBM . This allows to measure also the top of the valence band shift with the same offset procedure as in Hg 4f and Te 3d peaks, because the measurement of the valence band would be affected by all the problem of propagation of errors that affected the fitted core levels, and presents the problem of slope fitting. This process has an inherent error of 0.05 eV, which is very relevant if compared with the previously seen shift, which is less than double. However, measuring the core levels shift allows to introduce only 0.005 eV of error, making the measurement meaningful again.

This measurement confirm the rigid shift of all of the electronic structure to lower E_B , reaching around 0.1 eV in order of magnitude.

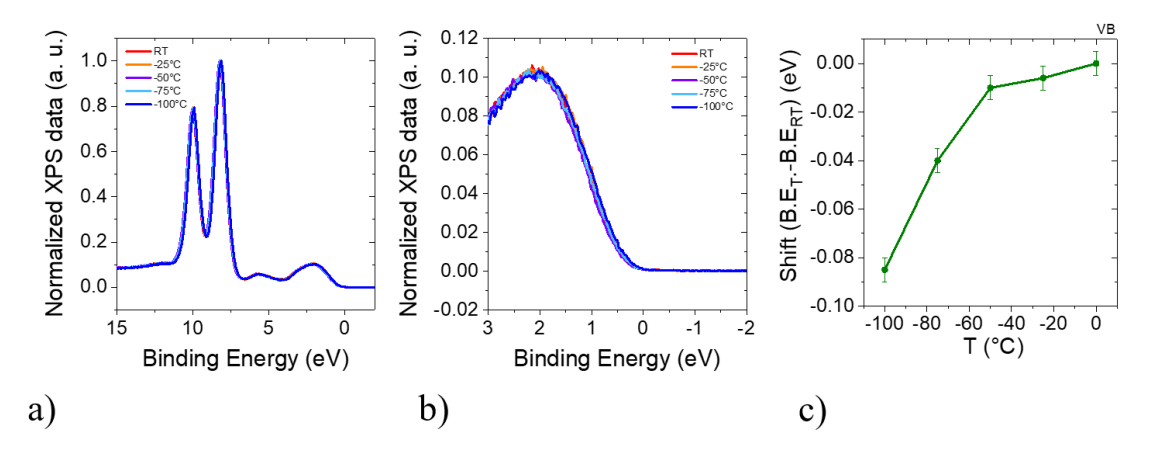


Figure 4.7: Variation of the 6k valence band with temperatures: a) Large range XPS measurement, b) detail of the valence band position with Respect to the Fermi level,c) Plot of the shift values

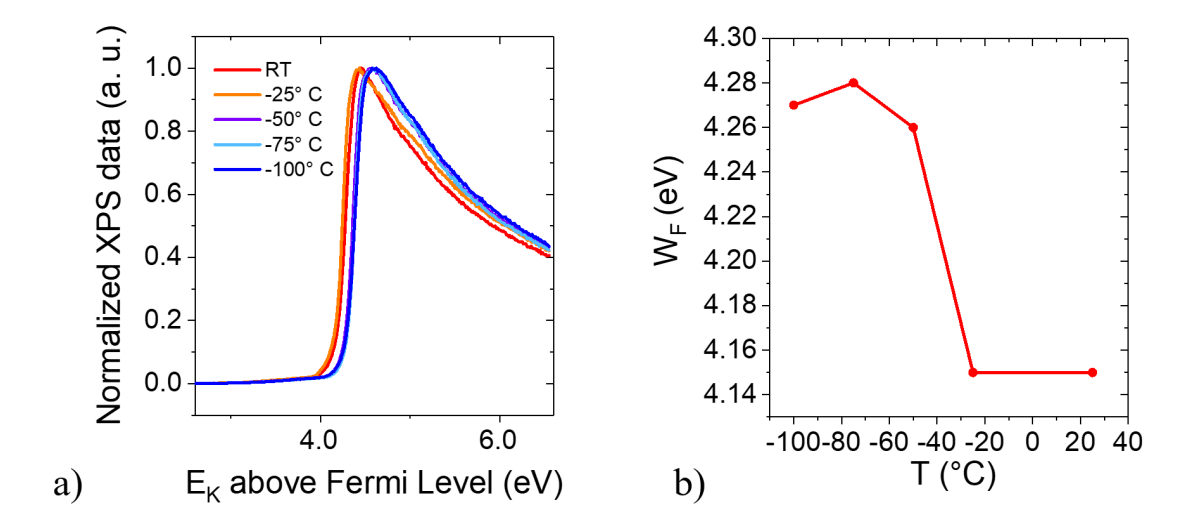


Figure 4.8: Variation of the 6k cut off with temperatures; comparison of the normalized values at different temperatures and plot of the values

The secondary electron cut offs follow a rather different behaviour, that needs more discussion. First of all, the value obtained is in accordance to the range reported in previous papers of the groups. However, the shift observed is not coherent with what was seen in the other measurements. It is in fact in the opposite direction, with an higher energy at lower temperature. It is clearly non linear, to the point that the shift observed at -75°C is more pronounced than the one observed at -100°C. And all this problems are evident from the initial comparison, and are not due to any additional error source introduced in the data treatment.

Control experiment: Au on Si substrate

No variation is observed at different temperatures on the clean substrate used as a control experiment: no shift of the core levels are seen, and the Fermi Level maintain its exact location 4.9. This allows to confirm that the shift observed in this case are intrinsic to the HgTE QDs film.

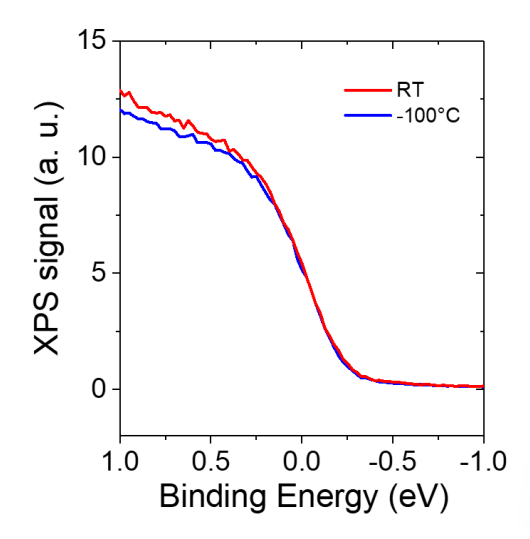


Figure 4.9: Fermi Level spectrum captured on Au on Si substrate at room temperature and at -100°C

3k and 4k samples

Identical procedures were applied for 3k and 4k films. These are QDs with a smaller band gap than the previous, and are thus even more interesting, because even with a smaller band gap shrink, the spectrum shift is as present as in the previous measurements on 6k.

The shift reported are remarkably comparable to the ones observed on the 6k sample. They have the same direction, and present the overall same behaviour. A small remark needs to be done; due to time constraints (longer range, longer acquisition time), it was not possible to take the valence band with its first peaks on the 4k sample and all the temperature, so thee shift is measured on the valence band feature in itself. This however did not impact too much the behavior of the results, because it still was possible to measure the shift by offsetting the measurements.

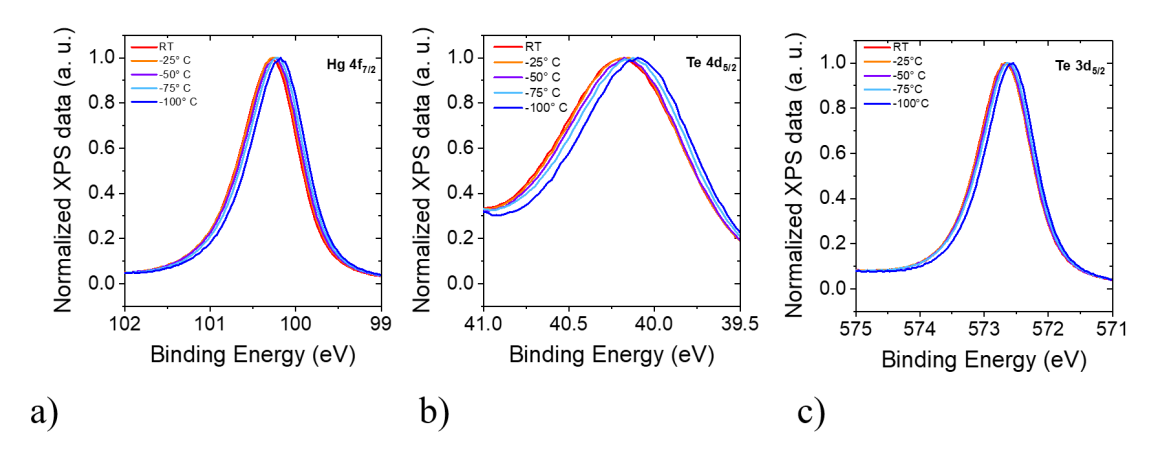


Figure 4.10: Variation of the 4k core levels with temperatures:a), b), and c) are zooms of the Low E_B feature of Hg 4f, Te 4d, and Te 3d

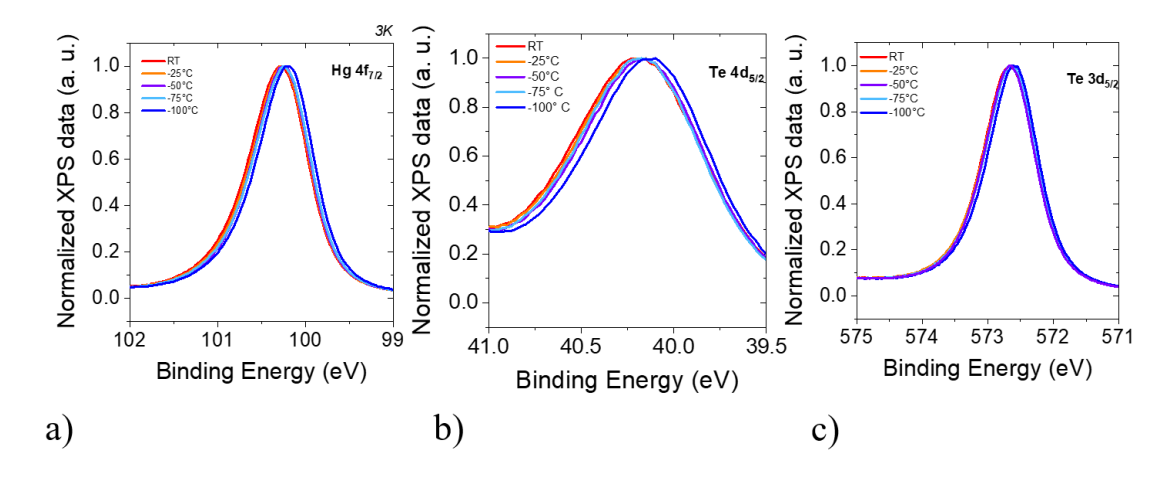


Figure 4.11: Variation of the 3k core levels with temperatures: a), b), and c) are zooms of the Low E_B feature of Hg 4f, Te 4d, and Te 3d

The measured work function of 4k (seen in figure 4.12) is of 4.6 eV of value, which usually spans between 4.2 eV[39] and 4. 6, find, while 3k sample has a measured work function of around 4.7 eV (figure 4.13). The cutoff of secondary electrons and thus the work function continue to not have a clear trend, and to not necessarily go to lower E_B . On 3k, the value seems to be slightly more overestimated. Also, even with repeated measurements it was not possible to eliminate the probably stray value at -25°C.

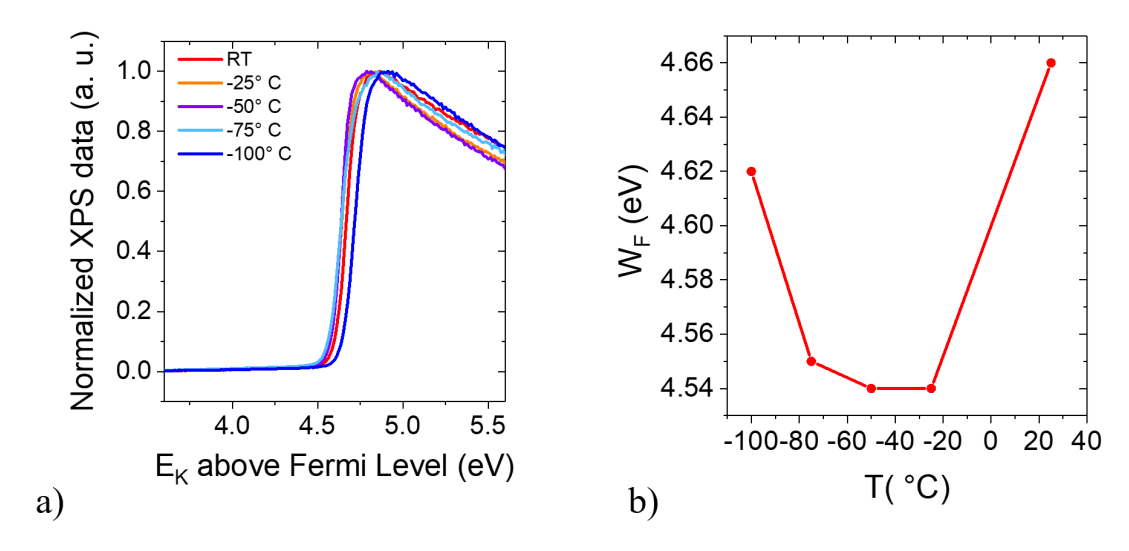


Figure 4.12: Variation of the 4k cut off with temperature and work function values plot

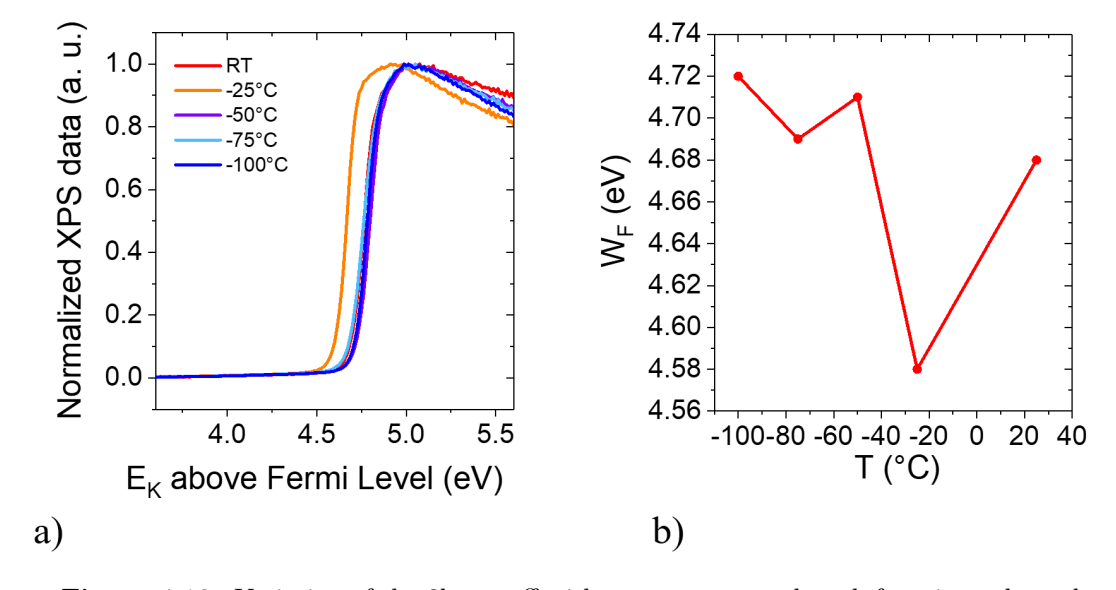


Figure 4.13: Variation of the 3k cut off with temperature and work function values plot

Reversibility of the process

The second measurement performed at room temperature, after the cooling process, confirms that the core levels fully recover their initial behaviour, as data shown in figure 4.14 are perfectly superimposable.

Understanding if the phenomena observed in temperature is due to a permanent modification of the material, or if it is reversible is a fundamental problem. It is important for applications, if there is a progressive modification of the behavior in time, the performance would be affected, and also to understand the physics of the process.

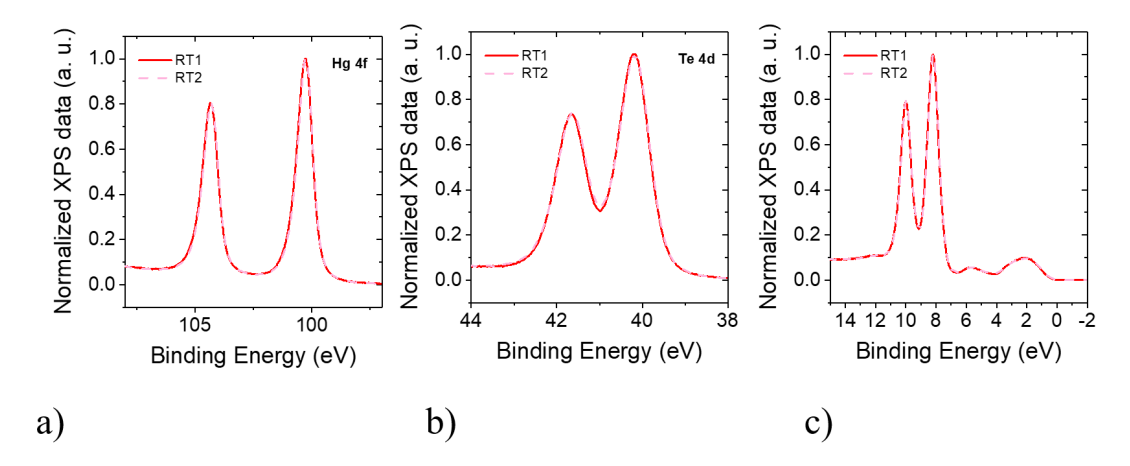


Figure 4.14: Measurements at room temperature taken before and after cooling

4.3 Results and discussion

4.3.1 Peaks and VB

As anticipated, and clearly evidenced in figure 4.15, 4.16 and 4.17, we have a pretty consistent behavior overall the whole QDs sizes: There is a shift, progressive with the temperature, but not linear, more pronounced from -75°C down. There is no clear size correlation evidenced; the shifts are overall always on the same trend, no size tend to have a more pronounced shift than the others, considering the 0.01 eV of the measurements.

In the end, is observed a shift of all the electronic core level to lower binding energies, closer to the Fermi level, of around 0.1 eV. This is a rather relevant quantity, compared to the starting band gap of the quantum dots, which are respectively around 0.37 eV (3k), 0.48 eV (4k), and 0.74 eV (6k).

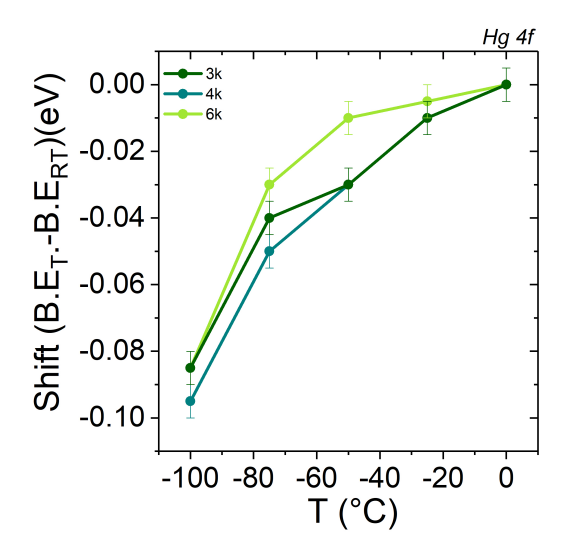


Figure 4.15: Shifts of the Hg 4f core level in temperature for all the sizes considered

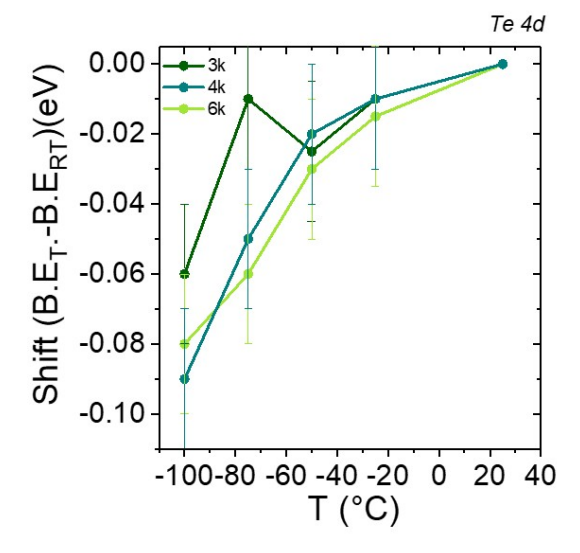


Figure 4.16: Shifts of the Te 4d core level in temperature for all the sizes considered

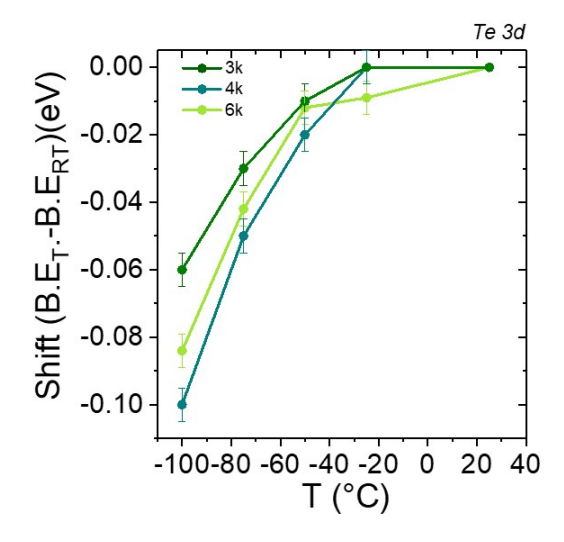


Figure 4.17: Shifts of the Te 3d core level in temperature for all the sizes considered

Valence band measurements performed on the three samples confirm the exact same trend that was evidenced for the peaks.

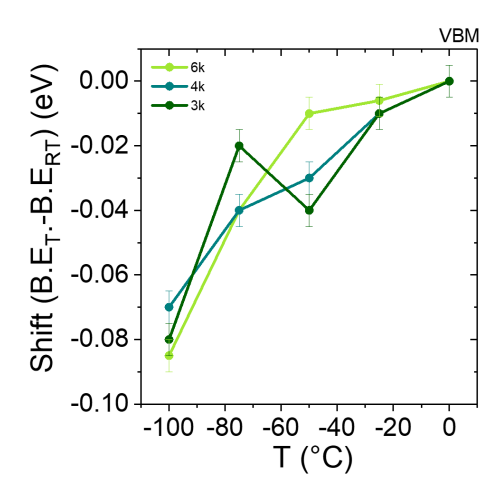


Figure 4.18: Shift of the valence band maximum in temperature for all the QDs sizes considered

There is slightly more variability, due to the more error that is present in the 4k measurement of VB, as discussed before. Additionally, this data do not take into account the small variations of temperatures, due to the use of a PID controller, and the possible reading error in the thermocouple. In the end, all the XPS spectrum, and thus all the electron-filled bands probed are undergoing a rigid shift to lower B.E, with no dependence on the size and band gap of quantum dots, even if this could have influenced their starting energy states. This means that for any of the QDs tested, we should expect the electronic levels to be a lot closer to the Fermi level than at room temperature. This shift is more pronounced at lower temperatures, it seems to almost activate and have an exponential behavior.

From the trend reported in figure 4.1 it was possible to have an estimation of the band gap shrinking of all the samples involved in this study. The behaviour of 6k and 4k had been experimentally tested, and 3k samples is expected to be on this same curve. It is recovered that 3k should shift of around 20 meV, 4k of 18, 6k of 16 meV. All these QDs present a band gap shrinking, due to the location of their k-states

This makes the shifts observed in photoemission all more impressive: for an expected band gap reduction of around 15-20 meV, a 100 meV shift is measured, roughly five times more.

With XPS, the electronic band structure of the filled electronic levels, so below the Fermi level, is probed, which is not recoverable from absorption measurements and had a very limited effect on the starting parameter of the $k \cdot p$ model. The rigid shift of the core levels and of the top of the valence band would suggest that all the lower electronic level are moving closer to the Fermi level. And they are shifting of a quantity that is far greater than the shift that is predicted in the kp model and is observed in absorption measurements. This adds new pieces to the understanding of the behaviour of the electronic structure in temperature.

Band diagram reconstruction

Using the band gap obtained from absorption measurements and the top of the valence band obtained with XPS measurements, it is possible to reconstruct the band diagrams shown in figure 4.19. In principle this could be made for all of the temperatures, however the most striking effect is for -100°C, and thus it was chosen to show this. The variation of the band gap shrinking observed in article are overall smaller than the error made in fitting the new data, so from now on the band gap shrinking will be rounded to 20 meV, with a slight overestimation. These band diagrams put into perspective the effects just observed: in fact the shift of the valence band, numerically almost the same for all the three QDs sizes, leads to very different effects on the totality of the band diagram, because the shift is more evident for smaller band gap. In fact, at room temperature both 4k and 6k have conduction and valence band almost equidistant from the Fermi level, this determines that the carrier population is dominated neither by hole neither by electrons. An example of this is evident in the section dedicated to electrical characterization in the first chapter. The band gap shrinks of approximately the 3% in 6k and 4% in 4k, and the change in the valence band is respectively of around the 11% of the band gap, and 17%. These are overall small variations, that do not create a substantial difference at -100°C. The ambipolar character is more or less maintained, with a Fermi Level that is still at the centre of the band gap. The behaviour is rather different for 3k, which is from the start dominated by n carriers, so with a conduction band closer to the electron Fermi level. The reduction is approximately of 5% and the VB shift of 22 % of the band gap. This determines the most evident effect, with the material conduction becoming less dominated by electrons and having a distance between CB and E_F more even to E_F and VB.

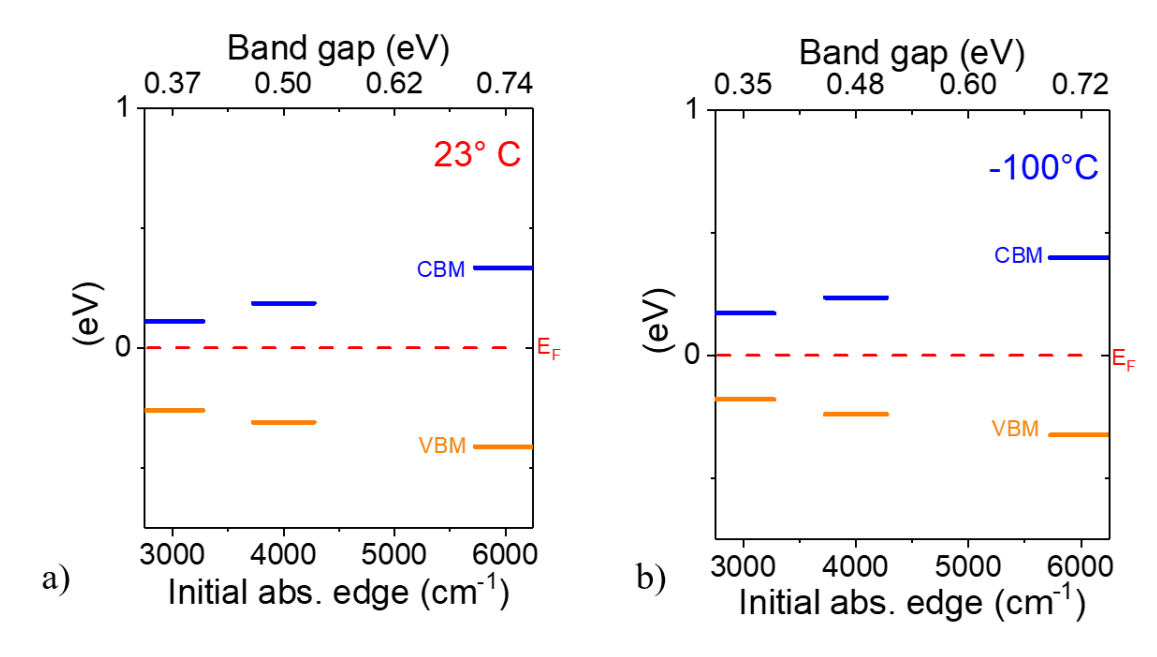


Figure 4.19: Band diagrams of the three quantum dots sizes at room temperature and at -100°C

In the specific 3k case, the trend observed can be confirmed also by previous experimental measurements performed in the lab, on the conductivity and mobility (similarly from section 1.3.5) of carriers performed in a criostate.

In this case, however, there is the necessity of using a dielectric gated transistor, because the electrolyte used is not compatible with operation below room temperature. The FET used in this case are constructed on a $Si\ SiO_2$ substrate, with gold electrodes, all covered by a spin-coated CQDs film. They present a back gate, and are not gated on the top as electrolyte-based FET. As evidenced in figure 4.20 b) at higher temperatures the transfer curve moves is shifted towards the negative side of V_{GS} , which means that the transport is dominated by n-carrier, the film act as an n doped channel. Going down to lower temperatures, there is a pretty defined change, with an ambipolar behaviour, with 0 current at $V_{GS}=0$, even if there are different slopes -and thus mobilities- of electron and holes. This appears to be in perfect accordance with the XPS data regarding this specific size of quantum dots, from which is possible to obtain more precise and quantitative information on the bands trends.

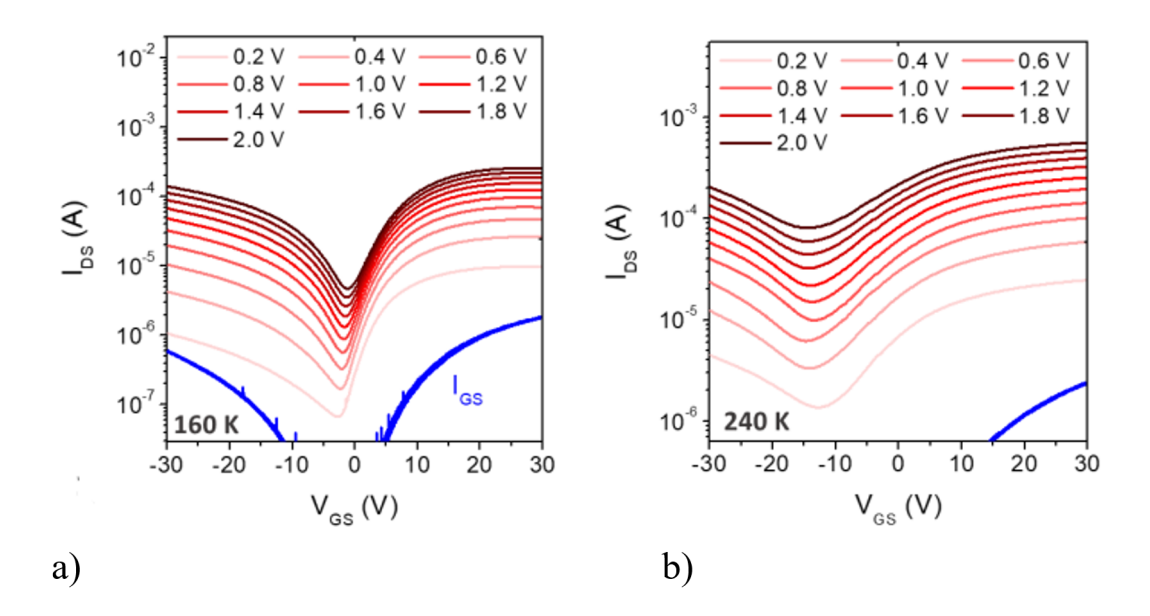


Figure 4.20: Curve of 3 k based transistor a) at around -100°C and b)at -30°C. Adapted from supporting information of [59]

4.3.2 Work function

The behaviour of the work function does not seem to follow the same rigid shift of the other two, and this is partially to be expected. They are very different types of measurement, based for example on primary and secondary electrons, and while the first allows to determine the position of the features with respect to the Fermi level, the latter allows to find the distance between the vacuum and the Fermi level.

No overall trend can be evidenced. The shift go in all directions, and this is evident from the very start, from the comparison of the raw data. This either opens the way to an interpretation of the vacuum level moving differently, or is due to some limit of the measurements

A source of error could come from the sensitivity of the work function to the machine electronics (cut-off is sampled with an applied bias), that potentially can be influenced by low temperatures. Cut-off is generally the measurement that on the machine can more easily create problems and not be perfectly reproducible. This still allows to evidence easily big shift of it, such as the one in chapter 3, that is around 0.2 eV, but could cover the smaller ones, if we expect this variation to be of the same magnitude as the core levels ones.

It also has to be fitted by determining the slope and the intersection with the zero signal, a type of measurement that has necessarily more data processing errors than the core level fit, for this reason it should be taken with a lot more carefulness than the others. The values found are, as anticipated, in accordance with the usual work function value reported. No trend can however be found, even if a modification of the values is observed. Only certainty is that the change on the work function cannot be caused by adsorption of other components, in this case. In fact, even if the cooling process cause a slight lowering of the pressure in the chamber, no new element or compound is found on the surveys taken at each temperature. The starting chamber is in ultra high vacuum and the films have undergone a long degassing process (around 8 hours), and remain in vacuum for the whole duration of the process.

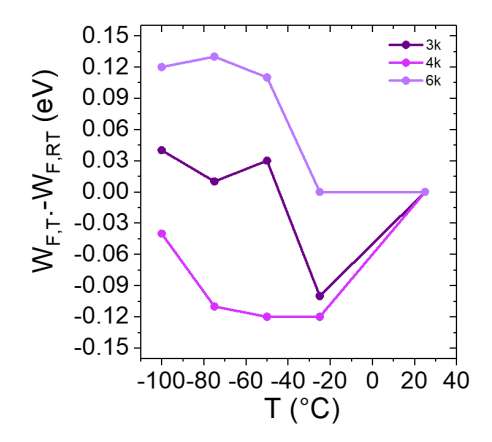


Figure 4.21: Shift of the work function in temperature for all the QDs sizes considered

Chapter 5

Conclusions

5.1 Conclusions

Specifically, the aim of this study was to determine how the parameters of the electronic structure of HgTe QDs, such as the work function and the energy difference between the valence band maximum and the Fermi level, evolve under varying experimental conditions.

In the first part of the investigation, the focus was placed on functionalization via alkali metal deposition, a technique previously demonstrated to lower the work function of thin films. This work sparked from earlier observations with potassium in HgTe QD films and extended them to include cesium. It was shown that cesium deposition induces a similar effect, and it was confirmed that the mechanism underlying the work function reduction stems from the creation of a surface dipole. Furthermore, it was observed that Cesium has a more pronounced effect for the same quantity of adsorbed atoms, and thus is an efficient proof of concept for this functionalization studies.

The second, and more novel, part of the research involved studying the temperature-dependent shift of the electronic structure using XPS, and thus probing the valence band location. These measurements revealed that, as temperature decreases, the valence band and core levels of the QD films shift closer to the Fermi level. This rigid shift, which reaches values of 0.1 eV at -100°C, is consistent across QDs of different sizes (3k, 4k, and 6k), and suggests a relevant change in the energy alignment of the bands.

Significantly, these shifts are much larger than the changes predicted solely by band gap narrowing from absorption spectroscopy (around 20 meV), and thus provide new perspectives on this phenomena.

In practical terms, this shift has important implications for QD based devices. For instance, in 3k QDs, which are more heavily n-type at room temperature, the shift results in a more ambipolar character at low temperatures. This prediction was confirmed by data on HgTe field-effect transistors observed at low temperatures. These findings highlight the importance of considering temperature effects in device design, especially for applications that operate at low temperature, such as infrared photodetector.

Lastly, this work also served a critical role in the validation of the newly arrived photoemission setup. The effectiveness of the transfer, and the process of temperature calibration, sample

handling, and instrumental stability under cooling were all evaluated and optimized. The successful execution of this study not only generated new data on HgTe QDs but also demonstrated the capabilities (and limitations) of the measurement set-up.

Appendix A

Background in XPS data: mathematical definition

Tougaard

Tougaard is the most correct from the physical point of view, relying on the quantitative description of the process implied in the photon scattering generation[60]. Nevertheless, it relies on a complex algorithm and on a precise knowledge of the material to determine the parameters inside it[35], so it is in practice never used in this report.

$$B(E) = \int_{E}^{\infty} K(E' - E) I(E') dE'$$
(A.1)

The energy loss function $K(\Delta E)$ is typically approximated as:

$$K(\Delta E) = \frac{A}{\Delta E^2 + B\Delta E + C} \tag{A.2}$$

Where $\Delta E = E' - E$ is the energy difference, A, B, C are empirical constants depending on the material, I(E') is the photoelectron intensity, point by point. It is thus possible only to calculate for well studied material.

Shirley background

Shirley background is simpler to calculate, needs less data, and is very useful in case a step is present [28], if the background before and after a peak presents as almost flat but at different heights.

$$B(E) = B(E_0) + [B(E_1) - B(E_0)] \cdot \frac{\int_E^{E_1} I(E') dE'}{\int_{E_0}^{E_1} I(E') dE'}$$
(A.3)

Where B(E) is the background intensity at binding energy E, $B(E_0)$ and $B(E_1)$ are the background values at the beginning and end of the peak region, I(E') is the measured spectral intensity at energy E'. Basically, this makes it so that the background is proportional in each point to the number of electrons with higher kinetic energy.

Appendix B

Supplementary information's on XPS acquisition

Survey

A survey taken with an Al source, 1486.6 eV of energy, is measured with $E_{pass} = 224$ eV and 0.8 eV of step, with range 1200-0 eV.

Core level

The three core level are taken with the following parameters:

- pass energy: 27 eV, step: 25 meV
- 3 sweeps (times in which the measurement is repeated and averaged) for Hg 4f and Te 3d, 8 for Te 4d

and the following Binding Energy ranges:

Table B.1: Peaks taken on the XPS set-up

Peaks	Window of acquisition
Hg 4f	115-95~eV
Te 3d	$595 - 565 \ eV$
Te 4d	$47 - 36 \; eV$

Valence Band

Valence band measurements are taken with the same pass energy and step (27 eV, 25 meV). Bigger range measurements, with the visible core levels, have range from 15 to -2 eV, and 5, -2 eV in the other cases.

Work function

The work function is taken with an applied bias of -10 V, pass energy $6.5~{\rm eV},$ step $12.5~{\rm meV},$ range $1477\text{-}1470~{\rm eV}.$

Bibliography

- [1] S. Ithurria, M. D. Tessier, B. Mahler, R. P. S. M. Lobo, B. Dubertret, and Efros A. L. «Colloidal nanoplatelets with two-dimensional electronic structure». In: *Nat. Mater* 10 (2011), p. 936 (cit. on p. 14).
- [2] Z. Q. Mamiyev and N. O. Balayeva. «Preparation and optical studies of PbS nanoparticles». In: *Optical materials* 46 (2015), pp. 522–525 (cit. on p. 14).
- [3] A W Beavis, M Jaros, A Zoryk, and I Morrison. «Electronic structure, effective masses and optical properties of perfect and imperfect HgTe-Hg1-xCdxTe and HgTe-Zn1-yCdyTe superlattices». In: 5, 10 (1990), p. 1051 (cit. on pp. 14, 21).
- [4] Al. L Efros and A. L. Efros. «Interband absorption of light in a semiconductor sphere». In: Fiz. Tekh. Poluprovodn. 16 (1982), pp. 1209–1214 (cit. on p. 15).
- [5] Y. Shu, X. Lin, Haiyan Qin, Zhuang Hu, Yizheng Jin, and Xiaogang Peng. «Quantum Dots for Display Applications». In: *Angewandte Chemie* 132 (2020) (cit. on p. 16).
- [6] E. Jang and H. Jang. «Review: Quantum Dot Light-Emitting Diode». In: *Chemical reviews* 123 (2023) (cit. on p. 16).
- [7] C. B. Murray, D. J. Norris, and M. G. Bawendi. «Synthesis and characterization of nearly monodisperse CdE (E = sulfur, selenium, tellurium) semiconductor nanocrystallites». In: *Journal of American Chemical Society* 115 (Sept. 1993), pp. 8706–8715 (cit. on p. 16).
- [8] L.E. Brus. «Electron-electron and electron-hole interactions in small semiconductor crystallites: The size dependence of the lowest excited electronic state.» In: *J. Chem. Phys.* 80 (1984), p. 4403 (cit. on p. 16).
- [9] A.I. Ekimov and A. A. Onushchenko. «Quantum Size Effect in Three-Dimensional Microscopic Semiconductor Crystals». In: Sov. J. Exp. Theor. Phys. Lett. 34 (Sept. 1981), p. 345 (cit. on p. 16).
- [10] C. Gréboval, A. Chu, N. Goubet, C. Livache, S. Ithurria, and E. Lhuillier. «Mercury Chalcogenide Quantum Dots: Material Perspective for Device Integration». In: *Chemical Reviews* 121 (2021), pp. 3627–3700 (cit. on pp. 20, 21, 55).
- [11] Council of European Union. Directive 2011/65/EU of the European Parliament and of the Council of 8 June 2011 on the restriction of the use of certain hazardous substances in electrical and electronic equipment. 2011 (cit. on p. 21).
- [12] A. Rogalski. «HgCdTe infrared detector material: history, status and outlook». In: Reports on Progress in Physics 68 (2005) (cit. on p. 21).
- [13] M. Penna, A. Marnetto, F. Bertazzi, E. Bellotti, and M. Goano. «Empirical Pseudopotential and Full-Brillouin-Zone k · p Electronic Structure of CdTe, HgTe, and Hg1-xCdxTe». In: *Journal of Electronic Materials* 38 (Nov. 2009), pp. 1717–1725 (cit. on p. 22).

- [14] K. A. Sergeeva et al. «The Rise of HgTe Colloidal Quantum Dots for Infrared Optoelectronics». In: Advanced functional materials 34 (2024) (cit. on p. 23).
- [15] H. Zhang et al. «Material Perspective on HgTe Nanocrystal-Based Short-Wave Infrared Focal Plane Arrays». In: *Chemistry of materials* 34 (2022) (cit. on p. 23).
- [16] M. Müllenborn, R. F. Jarvis Jr., B. G. Yacobi, R. B. Kanerand C. C. Coleman, and N. M. Haegel. «Characterization of solution-synthesized CdTe and HgTe». In: Solids And Materials 56 (1993) (cit. on p. 23).
- [17] A. Rogach, S. Kershaw, M. Burt, M. Harrison, A. Kornowski, A. Eychmüller, and H. Weller. «Colloidally Prepared HgTe Nanocrystals with Strong Room-Temperature Infrared Luminescence». In: *Advanced functional materials* 34 (2024) (cit. on p. 23).
- [18] H. Kim, K. Cho, B. Park, J. H. Kim, J. W. Lee, S. Kim, T. Noh, and E. Jang. «Optoelectronic characteristics of close-packed HgTe nanoparticles in the infrared range». In: Solid State Commun. 137 (2006) (cit. on p. 23).
- [19] M. V. Kovalenko, E. Kaufmann, D. Pachinger, J. Roither, M. Huber, J. Stangl, G. Hesserand, F. Schäffler, and W. Heiss. «Colloidal HgTe nanocrystals with widely tunable narrow band gap energies: from telecommunications to molecular vibrations». In: *Journal of the American Chemical Society* 128 (2006) (cit. on p. 23).
- [20] E. Izquierdo, A. Robin, S. Keuleyan, N. Lequeux, E. Lhuillier, and S. Ithurria. «Strongly Confined HgTe 2D Nanoplatelets as Narrow Near-Infrared Emitters». In: *Journal of the American Chemical Society* 138 (2016) (cit. on p. 23).
- [21] S. Bin Hafz, M. Scimeca, A. Sahu, and D. Ko. «Colloidal quantum dots for thermal infrared sensing and imaging». In: *Nano Convergence* (2019) (cit. on p. 23).
- [22] J. Qu et al. «Electroluminescence from nanocrystals above 2μm». In: Nature Photonics 16 (2021) (cit. on p. 23).
- [23] S. Keuleyan, E. Lhuillier, V. Brajuskovic, and P. Guyot-Sionnest. «Mid-infrared HgTe colloidal quantum dot photodetectors». In: *Nature photonics* 128 (2011), pp. 3516–3517 (cit. on p. 24).
- [24] R. Alchaar et al. «Focal plane array based on HgTe nanocrystals with photovoltaic operation in the short-wave infrared». In: *Applied Physics Letter* 123 (2023) (cit. on p. 24).
- [25] C. Gréboval et al. «Photoconductive focal plane array based on HgTe quantum dots for fast and cost-effective short-wave infrared imaging». In: *Nanoscale* 26 (2022) (cit. on p. 24).
- [26] C. Berglund and W. Spicer. «Photoemission Studies of Copper and Silver: Theory». In: Physical Review 136 (1964), A1030–1040 (cit. on p. 27).
- [27] H-Q Wang et al. «Determination of the embedded electronic states at nanoscale interface via surface-sensitive photoemission spectroscopy». In: *Light: Science Applications* 10 (2021), pp. 153–164 (cit. on p. 30).
- [28] G. Greczynski and L. Hultman. «A step-by-step guide to perform x-ray photoelectron spectroscopy». In: *Journal of Applied Physics* 132 (July 2022) (cit. on pp. 31, 40, 42, 78).
- [29] T. Schultz. «A unified secondary electron cut-off presentation and common mistakes in photoelectron spectroscopy». In: *Electronic Structure* 4 (Nov. 2022), p. 44002 (cit. on p. 33).
- [30] G. Allan and C. Delerue. «Tight-binding calculations of the optical properties of HgTe nanocrystals». In: *Physical Review B* 86 (2012) (cit. on p. 34).

- [31] M. Cavallo et al. «Mapping the Energy Landscape from an Nanocrystal-Based Field Effect Transistor under Operation Using Nanobeam Photoemission Spectroscopy». In: *Nanoletters* 23 (2023), pp. 1363–1370 (cit. on p. 36).
- [32] A. Khalili et al. «In Situ Mapping of the Vectorial Electric Field within a Nanocrystal Based Focal Plane Array Using Photoemission Microscopy». In: ACS: Applied electronic materials 5 (2023), pp. 4377–4384 (cit. on p. 36).
- [33] M. Cavallo et al. «Inside a nanocrystal-based photodiode using photoemission microscopy». In: Nanoscale 21 (2023) (cit. on p. 36).
- [34] S. Keuleyan, E. Lhuillier, V. Brajuskovic, and P. Guyot-Sionnest. «Mid-infrared HgTe colloidal quantum dot photodetectors». In: *Nature photonics* 5 (2011) (cit. on p. 37).
- [35] J. W. Pinder et al. «Avoiding common errors in X-ray photoelectron spectroscopy data collection and analysis, and properly reporting instrument parameters». In: Applied Surface Science Advances 19 (Jan. 2024), p. 100534 (cit. on pp. 40, 78).
- [36] J D Rogers, V S Sundaram, G G Kleiman, S G C Castroand R A Douglas, and A C Peterlevitz. «High resolution study of the M45N,7N67 and M47 Auger transitions in the 5d series». In: *Journal of Physics F: Metal Physics* 12 (1982) (cit. on p. 44).
- [37] V. I. Nefedov, Ya. V. Salyn, P. M. Solozhenkin, and G. Yu. Pulatov. «X-ray photoelectron study of surface compounds formed during flotation of minerals». In: *Surface and interface analysis* 2 (1980) (cit. on p. 44).
- [38] M. Scrocco. «X-ray photoelectron study of surface compounds formed during flotation of minerals». In: Journal of Electron Spectroscopy and Related Phenomena 50 (1990), pp. 171– 184 (cit. on p. 44).
- [39] D. Mastrippolito et al. «Tuning Electronic Properties of IIVI and IIIV Narrow Band Gap Nanocrystals through Exposure to Alkali». In: Chemistry of materials 36 (2024), pp. 11669– 11675 (cit. on pp. 44, 47, 55, 56, 67).
- [40] A.J. Strauss and R.F. Brebrick. «Vapor-crystal equilibrium and electrical properties of HgTe». In: *Journal of Physics and Chemistry of Solids* 31 (1970), pp. 2293–2307 (cit. on p. 45).
- [41] A. Jagtap et al. «Design of a Unipolar Barrier for a Nanocrystal-Based Short-Wave Infrared Photodiode». In: ACS Photonics 5 (2018) (cit. on pp. 45, 46).
- [42] M. Cavallo et al. «HgTe Nanocrystals Carrier Density and Its Tuning». In: *Small structures* (2025) (cit. on p. 45).
- [43] R. Bera, D. Choi, Y. S. Jung, H. Song, and K. S. Jeong. «Intraband Transitions of Nanocrystals Transforming from Lead Selenide to Self-doped Silver Selenide Quantum Dots by Cation Exchange». In: *Journal of Physical Chemistry letters* 13 (2022), pp. 6138–6146 (cit. on p. 45).
- [44] I. Ramiro, B. Kundu, M. Dalmases, O. Özdemir, M. Pedrosa, and G. Konstantatos. «Size-and Temperature-Dependent Intraband Optical Properties of Heavily n-Doped PbS Colloidal Quantum Dot Solid-State Films». In: ACS nano 10 (2020), pp. 7161–7169 (cit. on p. 45).
- [45] A. Sahu et al. «Electronic impurity doping in CdSe nanocrystals». In: *Nano letters* 12 (2012), pp. 2587–94 (cit. on p. 46).
- [46] A. H. Khan, V. Pinchetti, I. Tanghe, Z. Dang, B. Martín-García, Zeger Hens, D. Van Thourhout, P. Geiregat, and I. Moreels. «Tunable and Efficient Red to Near-Infrared Photoluminescence by Synergistic Exploitation of Core and Surface Silver Doping of CdSe Nanoplatelets». In: *Chemistry of materials* 31 (2019), pp. 1450–1459 (cit. on p. 46).

- [47] A. Chu et al. «HgTe Nanocrystals for SWIR Detection and Their Integration up to the Focal Plane Array». In: ACS Applied Materials Interfaces 11 (2019) (cit. on p. 46).
- [48] M.I. Trioni, S. Achilli, and E.V. Chulkov. «Key ingredients of the alkali atom metal surface interaction: Chemical bonding versus spectral properties». In: *Journal of Physics and Chemistry of Solids* 88 (2013), pp. 160–170 (cit. on p. 47).
- [49] E.M. Oellig and R. Miranda. «New experimental studies on the adsorption of K on Si(100) and Si(111)». In: Surface Science Letters 177 (1986), pp. 947–950 (cit. on p. 47).
- [50] D. M. Riffe, G. K. Wertheim, and P. H. Citrin. «Alkali metal adsorbates on W(110): Ionic, covalent, or metallic?» In: *Physical Reviews Letters* 57 (1990) (cit. on p. 47).
- [51] P. Senet, J.P. Toennies, and G. Witte. «Low-frequency vibrations of alkali atoms on Cu 001». In: Chemical Physics Letters 299 (1999), pp. 389–394 (cit. on pp. 48, 57).
- [52] G. Ebbinghaus and A. Simon. «Electronics structures of Rb, Cs and some of their metallic oxides studied by photoelectron spectroscopy». In: *Chemical Physics* 43 (1979) (cit. on p. 51).
- [53] J.H. Scofield. «Hartree-Slater subshell photoionization cross-sections at 1254 and 1487 eV». In: Journal of Electron Spectroscopy and Related Phenomena 8 (1976) (cit. on p. 54).
- [54] W.M.H. Sachtler, G.J.H. Dorgelo, and A.A. Holscher. «The work function of gold». In: Surface science 5 (1966), pp. 221–229 (cit. on p. 57).
- [55] H. L. Skriver and N. M. Rosengaard. «Surface energy and work function of elemental metals». In: *Physical Review B* 46 (1992) (cit. on p. 57).
- [56] K. P. O'Donnell and X. Chen. «Temperature dependence of semiconductor band gaps». In: *Applied physics letters* 58 (1991), pp. 2924–2926 (cit. on p. 59).
- [57] N. Moghaddam et al. «The Strong Confinement Regime in HgTe Two-Dimensional Nanoplatelets» In: The journal of physical chemistry C 124 (2020), pp. 23460–23468 (cit. on pp. 59–61).
- [58] E. Lhuillier, S. Keuleyan, and P. Guyot-Sionnest. «Optical properties of HgTe colloidal quantum dots». In: *Nanotechnology* 23 (2012) (cit. on p. 60).
- [59] T. H. Dang et al. «Nanocrystal-Based Active Photonics Device through Spatial Design of Light-Matter Coupling». In: *ACS photonics* 9 (2022) (cit. on p. 74).
- [60] S. Tougaard. «Practical guide to the use of backgrounds in quantitative XPS». In: *Journal of Vacuum Science and Technologies A* 39 (Jan. 2021), p. 011201 (cit. on p. 78).